heritage

Article

Non-Invasive Identification of Blue-And-White Porcelain: Comparison of Vietnamese, Yunnan and Jingdezhen Wares Using Reasoned Visualization and PCA

Philippe Colomban [1,*], Gulsu Simsek-Franci [2], Chun-Wei Chen [3], Han-Chun Hsieh [3] and Ching-Fei Shih [3]

[1] MONARIS UMR8233, Sorbonne Université, CNRS, Campus P.-et-M. Curie, 4 Place Jussieu, 75005 Paris, France
[2] Department of Metallurgical and Materials Engineering, Faculty of Chemical and Metallurgical Engineering, Yildiz Technical University, Davutpasa Mah. Davutpasa Caddesi, Esenler, 34220 Istanbul, Türkiye; gulsu.simsek@yildiz.edu.tr
[3] Graduate Institute of Art History, National Taiwan University, No. 1, Sec. 4, Roosevelt Road, Taipei 10617, Taiwan; chunwei@ntu.edu.tw (C.-W.C.); d15141002@ntu.edu.tw (H.-C.H.); shihcf@ntu.edu.tw (C.-F.S.)
* Correspondence: philippe.colomban@sorbonne-universite.fr

Abstract

The XRF, Raman, and fluorescence signatures of approximately fifteen blue-and-white and white porcelain sherds are compared. The assemblage comprises fourteenth- to sixteenth-century porcelain sherds, including Yuan and Ming wares from the Jingdezhen kiln sites, fifteenth- to sixteenth-century wares from the Yuxi and Jianshui kiln sites in Yunnan (China), and Vietnamese sherds comparable to ceramics recovered from the Cu Lao Cham (Hoi An) shipwreck preserved in private collections. Particular attention is paid to the XRF signals of impurities associated with sands (Zr, Y), fluxes (Rb, Sr), and cobalt-bearing ores (As, Mn, Fe, Ni, Bi), as well as to the Raman identification of specific phases in Chinese and Vietnamese porcelains. The similarity between Yunnan and Vietnamese blue-and-white wares is confirmed, notably by their high zirconium concentrations, whereas rubidium concentrations provide a means of distinguishing between the two regions. Overall, XRF signatures enable the non-invasive classification of the sherds according to their material characteristics. The resulting classifications are based on visualizations of clusters in the elemental compositional data using selected elements relevant to geological provenance and ceramic processing. These classifications are then compared with those obtained using PCA and hierarchical clustering based on Euclidean distances. Raman spectra highlight the presence of specific phases, including calcium silicates and phosphates. For the first time, particular emphasis is placed on the importance of considering the entire fluorescence spectrum as an identification tool. Special attention is given to the chromium fluorescence doublet with the α-alumina phase formed during the transformation from 2:1 mullite to 3:2 mullite at temperatures above 1200–1250 °C.

Keywords: porcelain; glaze; blue-and-white porcelain; blue; cobalt; yttrium; rubidium; strontium; zirconium; Jingdezhen; Vietnam; Yunnan; XRF; Raman microspectroscopy; chromium fluorescence; alumina; mullite; PCA

Check for updates

Academic Editor: Silvano Mignardi

Received: 13 August 2026
Revised: 30 August 2026
Accepted: 8 September 2026
Published: 10 September 2026

Copyright: © 2026 by the authors. Licensee MDPI, Basel, Switzerland. This article is an open access article distributed under the terms and conditions of the Creative Commons Attribution (CC BY) license.

1. Introduction

Blue-and-white porcelains constitute a major component of ceramic production in China, as well as in Vietnam and other parts of Asia and even Europe. Micro-destructive

analyses of excavated sherds have provided substantial knowledge, initially concerning ceramic bodies [1–4] (the number of publications is large; see the references therein), with more recent studies focusing on glazes and coloring agents, particularly Co^{2+} ions and the elements associated with this chromophore [5–42]. Analytical studies have addressed ceramic productions from the Tang [1,5,18], Song [1,19], Yuan [1,7,8,12,13,15,18–22,26,39,40], Ming [1,7,8,14,17,24], and Qing [7,23,31–35] dynasties. The production of replicas has proven to be one of the most effective approaches for validating analytical results [4,32]. As one of the major porcelain production centers, Jingdezhen has received extensive scholarly attention [3,6,7,11–15,19,20,22,23,27,33], making it impossible to cite all relevant analytical studies exhaustively. In contrast, analytical studies of Vietnamese [36–38] and Yunnan [38,41,42] blue-and-white porcelains remain much more limited. These studies have shown that, based on visual characteristics, porcelains produced in Vietnam and Yunnan are sufficiently similar to be easily confused. This similarity may partly reflect the location of the kilns within the broader Red River (Hong River) geological region, which could have contributed to the use of similar sand sources.

In the present work, we investigate a selection of fourteenth- to sixteenth-century archaeological sherds and specimens from private collections representing key blue-and-white porcelain production and archaeological contexts in Jingdezhen (JDZ), Yunnan (YN), and Vietnam (VTN). The Chinese samples are associated with the Jingdezhen kiln sites (see above mentioned references) and kiln sites in Yunnan [38,43–48], whereas the Vietnamese material comprises sherds comparable to the Cu Lao Cham shipwreck assemblage [36–38,49–51] and Chu Đau wares [36,51,52], sherds attributed to the Thăng Long Imperial Citadel [41,53–55], and a Vietnamese sherd from a surface find at Candi Kedaton, East Java [56]. For comparison, a Longquan celadon (L9) and a Qing-period (sample Q; Qianlong reign, Jingdezhen) ware were added to the corpus studied [57,58].

The analyses were carried out by combining inelastic Raman light-scattering micro-spectroscopy, used to identify crystalline and amorphous phases by considering both Raman vibrational spectra *stricto sensu* [59] and the associated fluorescence "background" [60–62] with X-ray fluorescence (XRF) spectroscopy for the comparison of elemental composition ratios [63]. Both techniques are non-invasive and can be implemented using mobile instruments in storage or exhibition environments [31–33,35,38,64,65].

By comparing samples associated with the Jingdezhen kiln sites, the Yuxi and Jianshui kiln sites in Yunnan, and Vietnamese blue-and-white wares, particular attention is paid to distinguishing the raw materials used for porcelain bodies, glazes, and blue decorations. This distinction is based not only on Raman vibrational spectra, but also on chromium fluorescence, and on the identification of impurities that yield significant XRF signals associated with the main raw materials: sands (Y, Zr), fluxes (Rb, Sr), and coloring ores (Co and the associated As, Mn, Fe, Ni, Bi, and Ti). The efficiency of these procedures is well established [5,11,12,16,18,23,30,33,65,66]. Specifically, (i) the relative proportions of specific impurities in sands (yttrium and zirconium) and fluxes (strontium and rubidium) have been shown to characterize raw material sources [65,66]; and (ii) cobalt and its associated elements in blue-decorated areas have long been investigated as indicators of cobalt sources [5,11,12,18,23,26,30,33,65]. Studies have also shown that, during the Yuan dynasty (1271–1368), cobalt imported from Persia (Iran) was associated with arsenic, whereas cobalt used during the early Ming dynasty (1368–before the Xuande reign, 1426–1435) was characterized by high iron and low manganese contents. After the Xuande reign, this trend was reversed, with higher manganese concentrations [11,14,23]. Several sources of so-called 'domestic' cobalt were identified after the Wanli reign (1572–1620), notably in the provinces of Zhejiang, Jiangxi, and Yunnan [16,18,66].

We will evaluate the potential of the fluorescence background for identifying the use of common raw materials, a potential that has recently been highlighted in studies of different ceramic productions [60–62].

2. Materials and Methods

2.1. Sherds

Table 1 lists the sherds examined in this study together with their selected characteristics and photographs. For several decades, excavations—whether terrestrial or underwater—have highlighted sources that were previously poorly documented, alongside benchmark productions such as those from Jingdezhen [67–71]. The assemblage comprises two white wares and four blue-and-white wares associated with the ancient Jingdezhen kiln sites (JDZ1–JDZ6, Jingdezhen, China); three blue-and-white sherds from surface finds at the Yuxi and Jianshui kiln sites in Yunnan (YN1–YN3, China) [40,41]; three Vietnamese blue-and-white sherds (VTN1–VTN3) stylistically and technically comparable to Chu Đau wares and ceramics recovered from the Cu Lao Cham (Hoi An) shipwreck [36–38,50–52,68]; and two blue-and-white sherds (TL1–TL2) attributed to surface finds from the Thăng Long Imperial Citadel [53,54].

Table 1. Provenance, sample labels, presumed production sites and dates (according to stylistic criteria), archaeological contexts, analytical techniques, and principal compositional characteristics of the studied specimens. References are provided where available.

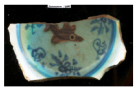
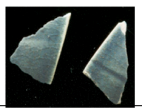
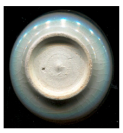
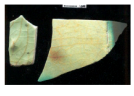
Kiln Place (Type)	Century	View	Label (Largest Dimension /cm)	Provenance (See Text)	Body	Glaze	Blue
Jingdezhen (Shufu)	14th		JDZ1 (12)	Jingdezhen, China	Rb-rich	Rb-rich	-
Jingdezhen (Shufu)	14th		JDZ2 (12)	Jingdezhen, China	Rb-rich	Rb-rich	-
Jingdezhen	Mid –14th		JDZ3 (9)	Jingdezhen, China	Rb-rich	Rb-rich	Fe-rich Mn-poor
Jingdezhen	Late 15th –Early 16th		JDZ4 (10)	Jingdezhen, China	Rb-rich	Rb-rich	Mn-rich
Jingdezhen	15th–16th		JDZ5 (7.5)	Jingdezhen, China	Rb-rich	Rb-rich	Mn-rich
Jingdezhen	15th –16th		JDZ6 (8)	Jingdezhen, China	Rb-rich	Rb-rich	Mn-rich

Table 1. *Cont.*

Kiln Place (Type)	Century	View	Label (Largest Dimension /cm)	Provenance (See Text)	Body	Glaze	Blue
Yunnan	15th –16th		YN1 (6.5)	Yuxi kiln site, Yunnan, China	Sr-rich Zr-rich	Sr-rich Zr-rich	Mn-rich
Yunnan	15th –16th		YN2 (12)	Yuxi kiln site, Yunnan, China	Sr-medium Zr-rich	Sr-medium Zr-rich	Mn-rich
Yunnan	15th		YN3 (6)	Jianshui kiln site, Yunnan, China	Sr-rich Zr-rich	Sr-rich Zr-rich	Mn-rich
Vietnam	15th		VTN1 (5)	Surface find, Candi Kedaton, East Java	Zr-rich	Sr-rich Zr-medium	Fe-rich
Vietnam	Late 15th –Early 16th		VTN2 (1.8)	Cu Lao Cham (Hoi An) Shipwreck, Vietnam	Not measured	Not measured	Not measured
Vietnam	Late 15th –Early 16th		VTN3-A (4.7) Lid	Cu Lao Cham (Hoi An) Shipwreck, Vietnam	Zr-rich	Rb-medium Sr-medium Zr-medium Mn-rich	Mn-rich
Vietnam	Late 15th –Early 16th		VTN3-B (4.5) Base	Cu Lao Cham (Hoi An) Shipwreck Vietnam	Zr-rich	Rb-medium Sr-medium Zr-medium Mn-rich	Mn-rich
Vietnam	15th		SD TL1 (3.6)	Surface find, Thăng Long Imperial Citadel, Vietnam	Rb-rich Zr-rich	Rb-medium Sr-medium	Mn-rich
Vietnam	Late 15th –Early 16th		GD TL2 (5.8)	Surface find, Cu Lao Cham shipwreck, Vietnam	Rb-rich	Rb-medium	Mn-rich
Jingdezhen	18th		Q (fragment: 2)	European market	Rb-rich	Rb-rich	As-rich
Longquan	14th		L9 (9)	Sicao, Tainan, Taiwan	Rb-rich	Sr-rich	-

The JDZ1–JDZ6, YN1–YN3, and VTN1–VTN3 specimens are from the study collection of the Fine Arts Museum, Graduate Institute of Art History, National Taiwan University, whereas the TL1–TL2 specimens are from a private collection.

JDZ1 and JDZ2 are Yuan Shufu (樞府)-type white ware dishes with molded floral decoration, comparable to fourteenth-century white wares with molded chrysanthemum decoration recovered from the Tuchengzi city site, Ulanqab, Inner Mongolia [69],

and from the Shexian hoard, Anhui Province [70]. Excavated artifacts from the Hutian kiln site in Jingdezhen demonstrate the evolution of local ceramic production from *qingbai* (青白, bluish-white) ware through Shufu (樞府)-type white ware to blue-and-white porcelain from the Song to the Ming dynasties. These wares were occasionally produced contemporaneously, even within the same kiln complex [71]. Shufu (樞府)-type white ware is characterized by an opaque, milky-white glaze and by the molded characters *Shu* (樞) and *Fu* (府), which are frequently impressed on the interior surface and are generally regarded as an abbreviation for a Yuan government office [72].

JDZ3 is a late Yuan (mid-fourteenth-century) blue-and-white bowl base decorated with a floral motif. Comparable sherds have been recovered from archaeological sites, including Fustat in Egypt, where they have been dated to the second half of the fourteenth century [73]. JDZ4 is the base of a blue-and-white dish with an unglazed applied fish motif. Comparable examples have been recovered from the Jingdezhen kiln site [74] and from a Ming-dynasty tomb in Hubei Province dated to 1525, suggesting a date between the late fifteenth and early sixteenth centuries [75]. JDZ5 is a blue-and-white sherd decorated with the *shou* (壽, longevity) character. A similar example, dated to the late fifteenth to the sixteenth century, is a blue-and-white dish recovered from the Klang Ao shipwreck in the Gulf of Thailand [76]. JDZ6 is a blue-and-white sherd decorated with plum blossoms and a crescent moon. Comparable examples have been recovered from fifteenth- to sixteenth-century archaeological sites in the Philippines [44,77,78] (pp. 235–268).

YN1–YN3 are surface finds from the Yuxi and Jianshui kiln sites in Yunnan. YN1 is a blue-and-white sherd decorated with a pavilion motif from the Yuxi kiln site, Yunnan Province [78]. It can be dated to the fifteenth to sixteenth century based on comparisons with similar motifs on Jingdezhen blue-and-white wares and with an excavated example from a Ming tomb in Gejiu(箇舊), Yunnan Province [44]. YN2 is a blue-and-white sherd decorated with a fish-and-aquatic-plant motif from the Jianshui kiln site, Yunnan Province. The fish-and-aquatic-plant motif is one of the most common decorative motifs on Yunnan blue-and-white wares and is well represented among finds from kiln sites, tombs, and museum collections [44] (pp. 235–268). YN3 is a blue-and-white sherd decorated with floral scrolls and stylized lotus petals from the Jianshui kiln site, Yunnan Province. Comparable examples include one excavated from Lufeng (祿豐), Yunnan Province, which, based on stylistic development, has been dated to the fifteenth century [44] (pp. 235–268).

VTN1 is a blue-and-white sherd from a surface find at Candi Kedaton, East Java. Its floral motif against a cross-hatched background is comparable to that of a fifteenth-century Vietnamese blue-and-white *yuhuchunping* (pear-shaped) bottle excavated from the Kyo no Uchi site of Shuri Castle, Okinawa [79]. VTN2 consists of cobalt-blue-glazed sherds from a small covered box with a molded twelve-petalled floral cover. Comparable Vietnamese examples have been recovered from the Cu Lao Cham island shipwreck near Hoi An, a major trading port in central Vietnam during the Cham and early Vietnamese periods. Most of the Vietnamese ceramics recovered from the shipwreck are attributed to the Chu Đau kilns and date to the late fifteenth to early sixteenth century [36–38]. VTN3 is a small blue-and-white covered box decorated with a central medallion surrounded by concentric circular bands and a border of stylized petals. Comparable Vietnamese covered boxes have also been recovered from the Cu Lao Cham shipwreck.

TL1 and TL2 are two small blue-and-white sherds from surface finds at the Thăng Long Imperial Citadel, Hanoi, Vietnam [53,54]. TL1 is a blue-and-white sherd decorated with a small simplified five-clawed dragon-and-cloud motif (SD), comparable to fifteenth-century examples excavated from the Imperial Citadel of Thăng Long, Hanoi [53,54]. TL2 is a tiny blue-and-white sherd preserving the lower part of a bird motif.

The preserved curved claws correspond closely to those on Vietnamese blue-and-white vases recovered from the Cu Lao Cham shipwreck [36–38,49–52].

2.2. Methods

2.2.1. Raman Microspectroscopy

Raman spectroscopic measurements were performed using a LabRAM HR800 Raman microspectrometer (HORIBA Scientific Jobin-Yvon, Palaiseau, France), equipped with an Ar^+ ion laser (Innova I90C 6UV, Coherent Inc., Santa Clara, CA, USA). Excitation was provided by the 514.5 nm laser line. The spectrometer was calibrated using the silicon band at 520.5 cm^{-1} before each measurement. The laser power at the sample ranged from approximately 0.5 mW for dark-colored areas to 20 mW for colorless zones. Micro-Raman analyses were carried out using Olympus (Tokyo, Japan) long-working-distance (LWD) 50x and 10x objectives, providing spot sizes of approximately 5 × 5 μm^2 and 30 × 30 μm^2, respectively. The laser penetration depth was approximately less than twice as great in colorless glazes but was significantly reduced in dark-colored areas. Indeed, the optimization of microscope optics aims to achieve high spatial resolution in the xy-plane; consequently, in a transparent medium, the shape of the spot is elongated along the *z*-axis, which degrades spatial resolution in that direction.

Spectra were collected over the range 20–8000 cm^{-1}, with acquisition times varying from a few minutes to several tens of minutes depending on signal intensity. At least three accumulations were recorded for each spectrum to eliminate cosmic-ray spikes. All spectra in the 4000–8000 cm^{-1} region were acquired under identical conditions (10 mW laser power at the sample, 180 µm confocal hole, 50x objective, 3 s acquisition time, and 10 accumulations) to ensure comparability. As the fluorescence components—as we shall see—serve as a source of information, no spectral modifications, such as baseline subtraction or smoothing, are performed.

2.2.2. Portable X-Ray Fluorescence Spectroscopy (pXRF)

The analytical protocol followed the procedures described in previous studies [32,33,35,78,80,81]. XRF analyses were performed using portable ELIO X-ray fluorescence (XRF) spectrometers (first-generation ELIO, Milano, Italy; second-generation, Bruker NanoAnalytics, Berlin, Germany). Regarding the acquisition of spectra, the two instruments have similar spectral resolution; the main difference is the lower number of counts per counting period obtained with the second-generation instrument. The second-generation instrument is equipped with a Rh-anode X-ray tube, a ~1 mm^2 collimator, and a large-area silicon drift detector (SDD) incorporating CUBE low-noise CMOS preamplifier technology (energy resolution < 140 eV for Mn Kα; detection range: 1.3–43 keV in air).

The instrument was mounted on a dedicated frame to ensure stability during measurements. Analyses were performed in point mode with an acquisition time of 180 s at 50kV and 80 µA, without a filter between the X-ray tube and the sample. The analysis depth, estimated using the Beer–Lambert law and defined as the depth from which 90% of the fluorescence signal originates, was approximately 6 µm for Si Kα (1.740 keV), 170 µm for Cu Kα (8.048 keV), 300 µm for Au Lα (9.713 keV), and up to 3 mm for Sn Kα (25.27 keV) [82,83]. Typically, the glaze thicknesses range between 200 and 500 µm [24,36–38]. Instrument accuracy was verified using reference glass and stone materials.

Because the intensity of characteristic X-ray emission peaks (Kα, Kβ, Mα, Mβ, Lα, Lβ, Lγ, etc.) [82,83] depend on elemental identity, concentration, and matrix absorption effects, peaks associated with trace elements such as Pb or Rb may appear visually more intense than those of major constituents such as Si. Furthermore, due to heterogeneous

variations in the three-dimensional distribution of colorants and the stratigraphy of glaze layers, calculation of a single representative "composition" is not meaningful. Instead, a clustering approach developed by our group was adopted. This method consists of plotting peak areas, calculated using Artax software (version 7.4.0.0, Bruker AXS GmbH, Berlin, Germany), in ternary and biplot scatter diagrams. Normalization was performed relative to the Rh tube peak to minimize variations arising from differences in artifact shape and the relative positioning of the instrument. For blue-decorated areas, peak areas were additionally normalized to the Co signal, allowing comparisons across different chronological periods and technological contexts.

Ternary scatter diagrams were generated for data interpretation and discussion using Statistica® version 14.1.0.8 (1984–2023 Cloud Software Group, Inc., Fort Lauderdale, FL, USA). The same software was also used to perform principal component analysis (PCA) based on elemental variables normalized to the Rh tube peak. In Statistica®, the plot case factor coordinates option was selected for PCA visualization.

For hierarchical clustering (similarity) analysis, the dataset was first explored using the Pandas library. Agglomerative clustering was then performed using the Agglomerative Clustering class from the sklearn.cluster® module. Dendrograms were generated to visualize the composition of each cluster and the relative distances between specimens. Ward's method was selected as the linkage criterion and implemented using the spicy.cluster.hierarchy® module, while matplotlib® was used for plotting. All calculations were performed in a JupyterLab® environment (version 4.1.6).

3. Results

The simplest procedure is the visual analysis of the spectra. Good spectral resolution is essential because, owing to the very strong coloring power of some ions, the XRF signals of certain elements are often very weak and may be superimposed on peaks from other elements. Therefore, before any quantitative comparison of signal intensities using the instrument software, it is necessary to verify that the element is actually present and to exclude measurements from areas affected by surface corrosion, which can distort the measurements of elements such as Si, Al, K, and Ca, as well as from areas where the glaze thickness is less than 300 μm, which can affect the measurement of heavy elements such as As, Pb, and close to millimeter(s) for Sn and Sb [78,80].

3.1. XRF Analysis of Body and Glaze Elemental Composition

Figures 1–5 present a selection of the most representative XRF spectra. Visual comparison of the spectra generally allows similar and distinct signatures to be readily identified. For example, clear differences can be observed between the JDZ3 and YN1 spectra and between the JDZ6 and VTN1 spectra, whereas the JDZ6 and JDZ5 spectra are closely similar, as expected for productions from the same location. The discussion focuses on the relative intensities of the characteristic Kα peaks of potassium and calcium around 4 keV, as well as on impurity-related elements detected between 14 and 18 keV, namely Rb, Y, Sr, and Zr, for all analyzed areas (porcelain body, colorless glaze, and blue-colored glaze). Additional attention is paid to impurities such as Ti and V detected in the 5–6 keV range [83].

The relative intensities of major elements (K and Ca) and trace elements allow different ceramic bodies and glazes to be discriminated according to their composition and raw materials. In blue-decorated areas, particular attention is given to the relative intensities of Mn, Fe, Ni, and As, which are associated with cobalt in varying proportions depending on the geological origin of the cobalt source [18,84–89].

It should be noted that, given the energy resolution of the instrument, separation of the Fe Kβ line (7.06 keV; with an intensity approximately one-fifth that of the Fe Kα line at

6.41 keV) from the Co Kα line (6.93 keV) is visually difficult [83]. When the intensities of the two lines are comparable, they may appear as a single broadened peak; when one is weaker, the resulting peak asymmetry must be examined. However, spectral deconvolution using Artax software allows reliable fitting and comparison of these overlapping signals.

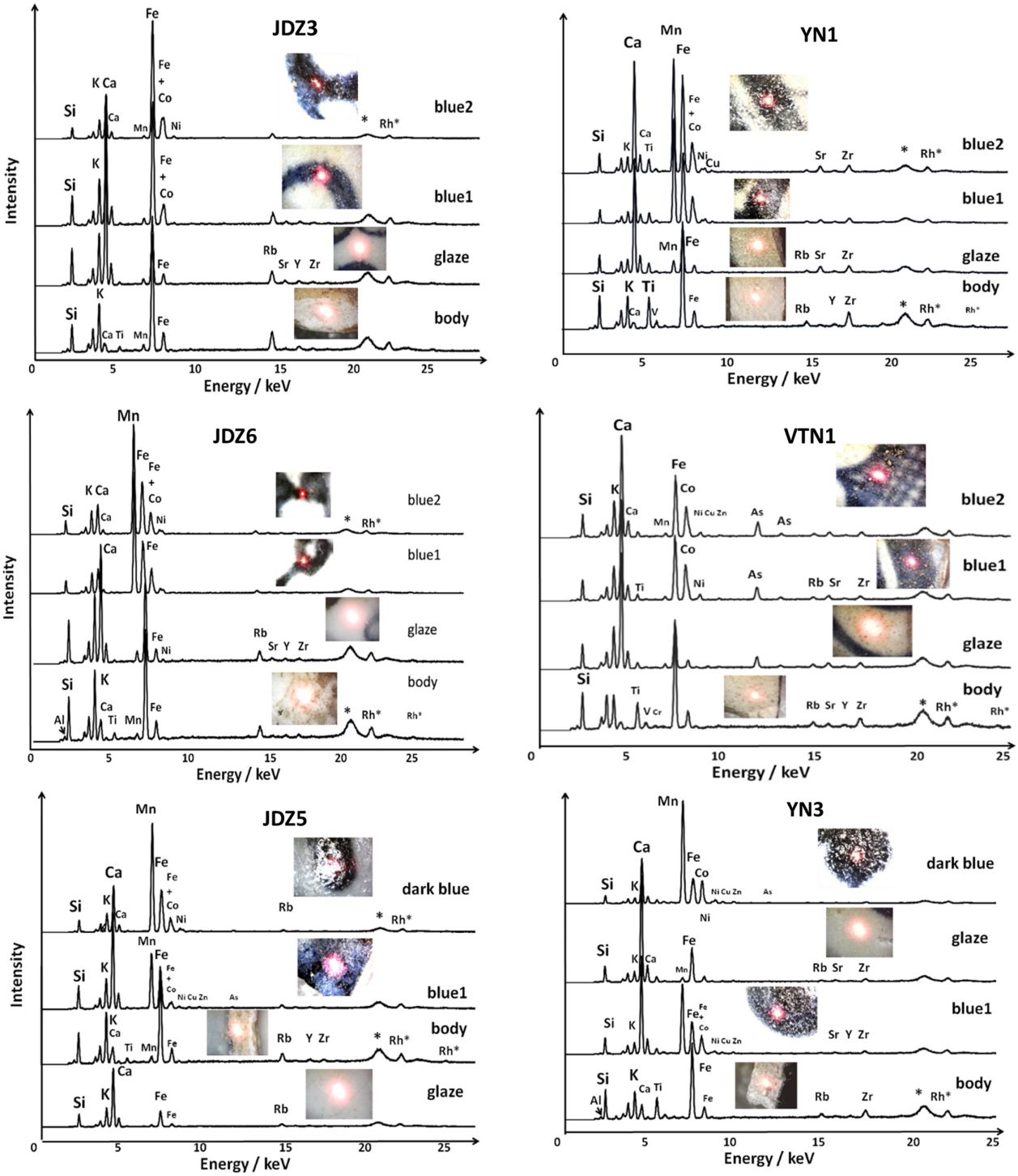


Figure 1. Representative XRF spectra recorded on various colorless and colored glazed zones and on the ceramic bodies of blue-and-white sherds (JDZ3, JDZ5, JDZ6, YN1, YN3, and VTN1). An optical image of each analyzed spot is also provided (measurements with the first-generation Elio instrument). (*: Compton scattering and rhodium source peaks).

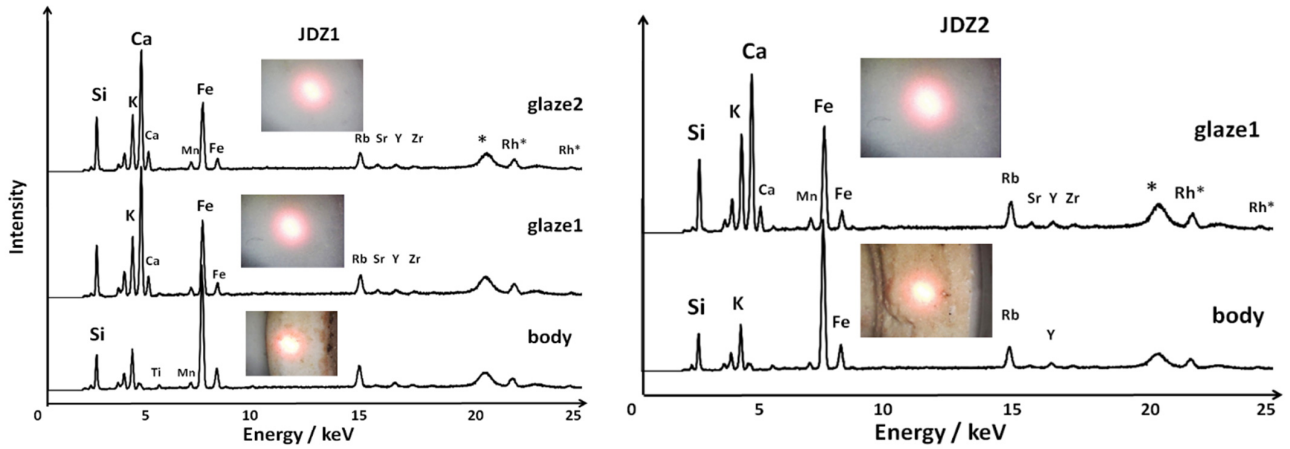


Figure 2. Representative XRF spectra recorded on glazed areas and ceramic bodies of Jingdezhen celadon sherds (JDZ1 and JDZ2) (measurements with the first-generation Elio instrument). (*: Compton scattering and rhodium source peaks).

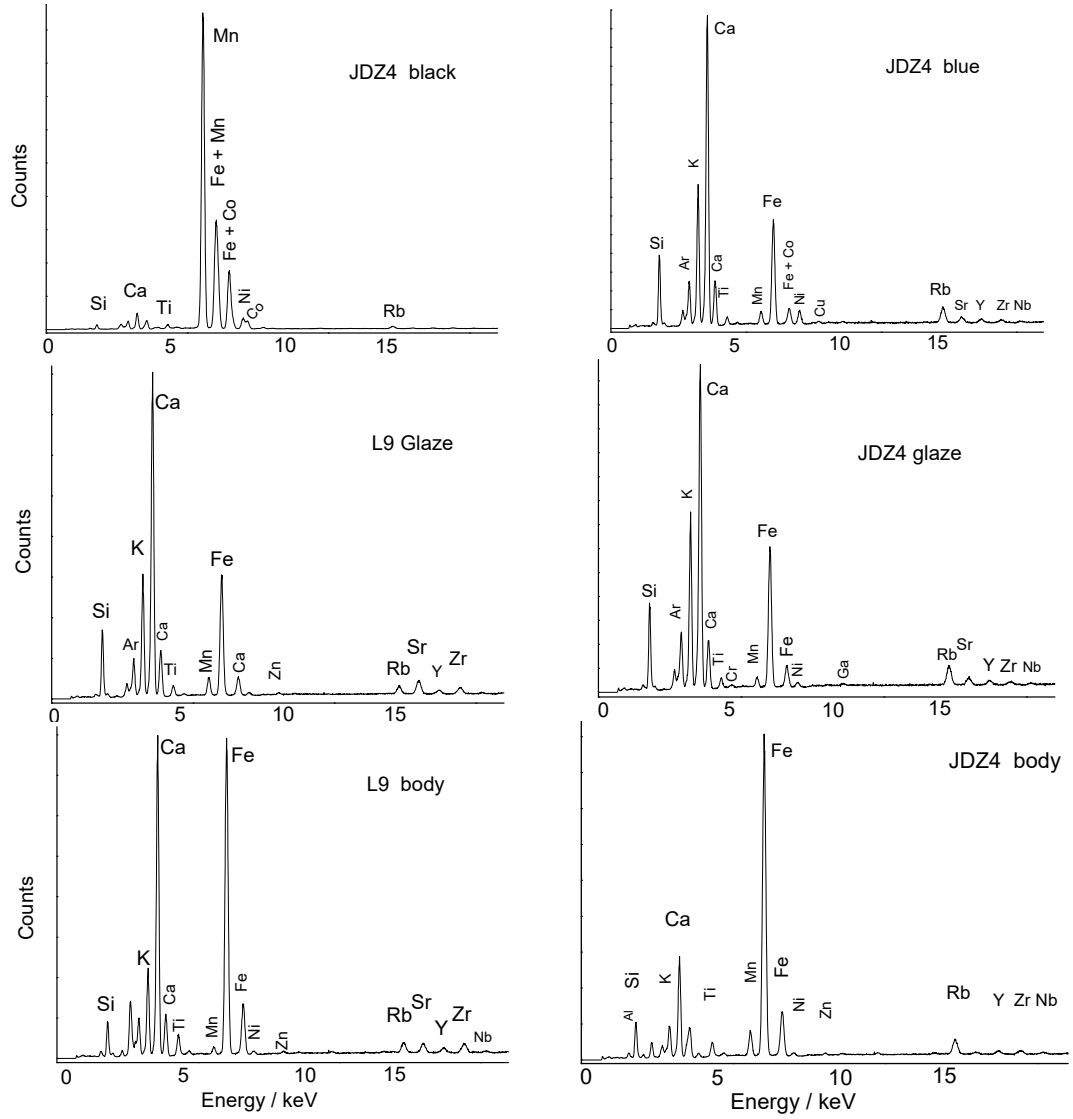


Figure 3. Representative XRF spectra recorded on various colorless and colored glazed areas and on the ceramic bodies of blue-and-white sherds (L9 and JDZ4) (measurements with the second-generation Elio instrument).

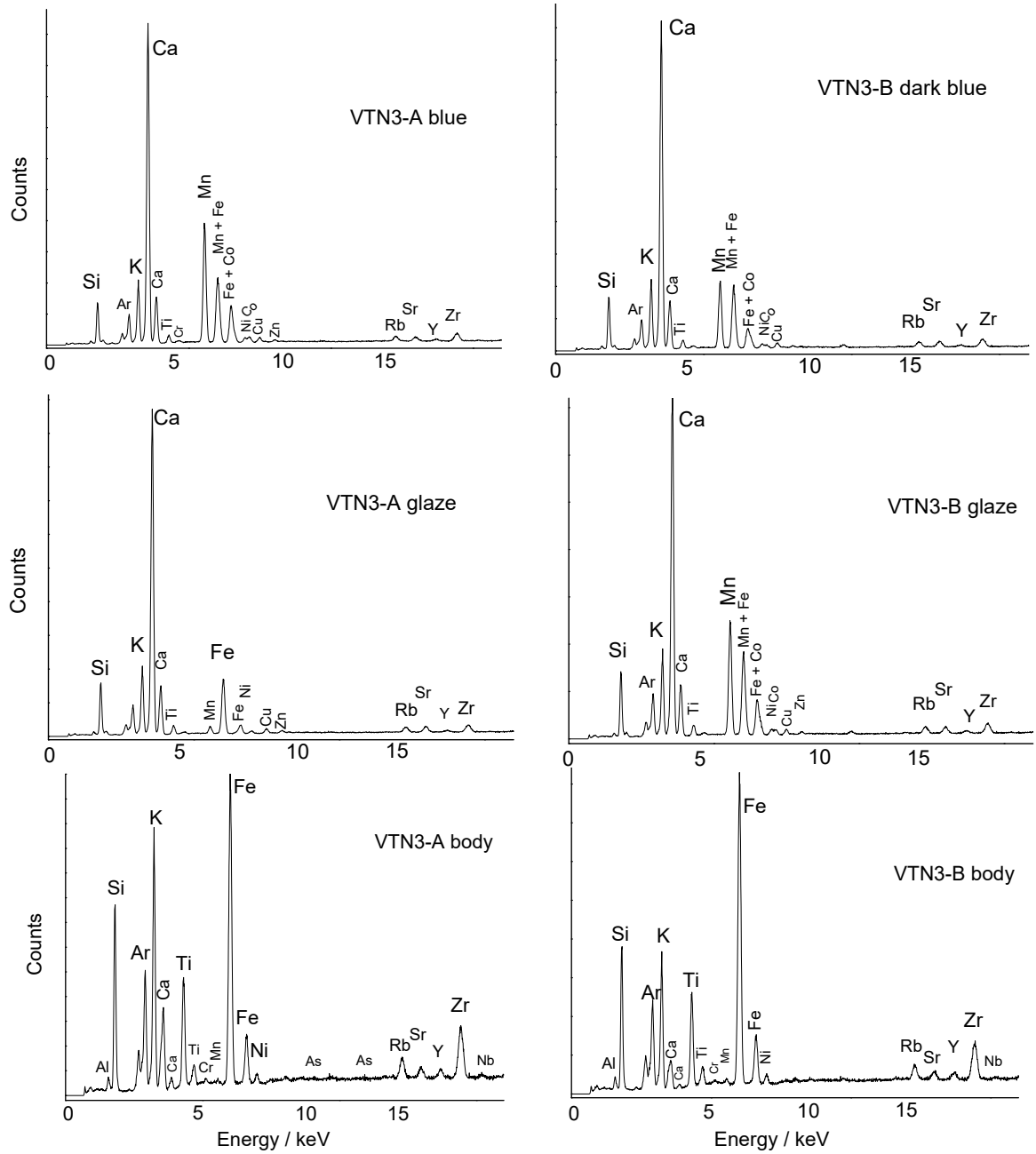


Figure 4. Representative XRF spectra recorded on various colorless and colored glazed zones and on the body of a blue-and-white VTN3 box (A: lid; B: base) (measurements with the second-generation Elio instrument).

3.1.1. Major Elements of Body and Glaze

Porcelain bodies are characterized by potassium peaks that are more intense than the corresponding calcium peaks. However, visual differentiation of the ceramic bodies is difficult based on these major elements alone (Figures 1–3), although the relative intensities of some impurity elements (Ti, V, and Mn) provide additional discriminatory information.

The bodies of JDZ1 and JDZ2 (14th c.), from Jingdezhen, together with those of YN1 and YN2 (15/16th c.), attributed to Yunnan kilns, show relatively similar compositional signatures. In contrast, JDZ3 (mid-14th c.), JDZ5 (15th/16th c.), and JDZ6 (15/16th c.), also attributed to Jingdezhen kilns but dating to different periods, exhibit a distinct compositional signature. This compositional criterion, based solely on the relative intensities of K and Ca peaks, is therefore insufficient to reliably identifying production origins. Two groups can

also be distinguished for the glaze compositions: one comprising the JDZ sherds and a second comprising the Yunnan samples together with TL2.

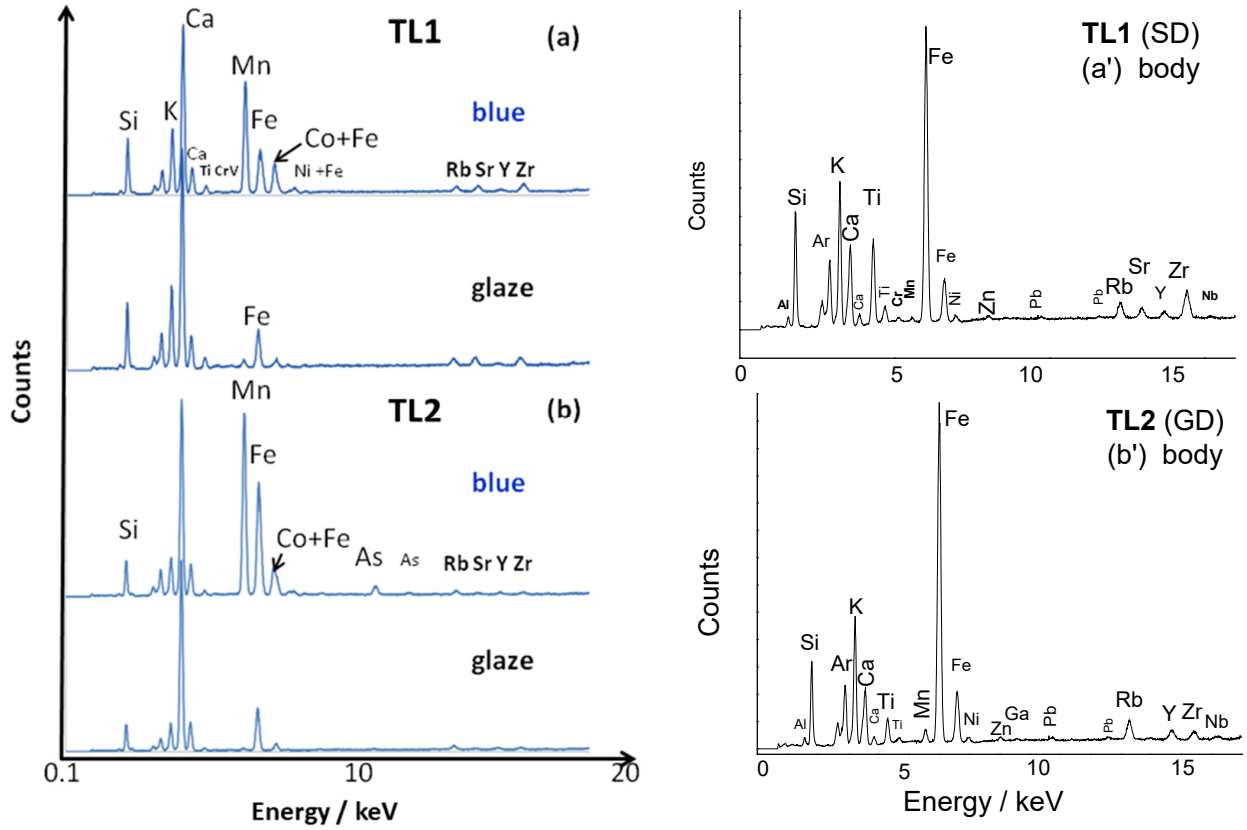


Figure 5. Representative XRF spectra recorded on blue and colorless glazed areas and on the bodies of the SD (TL1) (**a**,**a′**) and GD (TL2) (**b**,**b′**) sherds) (measurements with the second-generation Elio instrument).

3.1.2. Trace Elements of Body and Glaze

Identification of common raw materials is possible through comparison of the signals of selected impurity elements [30–36,38,65,66]. Signals corresponding to Rb, Sr, Y, and Zr, and occasionally U and Nb, are sufficiently intense to be visually detected by X-ray fluorescence spectroscopy, despite these elements being present only at trace levels. Rubidium is typically associated with sodium- and potassium-bearing raw materials, strontium with calcium-bearing raw materials, and zirconium and yttrium with quartz-rich sands, commonly occurring in the form of zircon. Visual inspection of the spectra shows that the relative intensities of these trace elements vary significantly among the samples.

Examination of Figures 1–5 highlights significant variations in the relative intensities of the Rb, Sr, Y, and Zr peaks. As previously observed in studies of porcelains from the Chu Đau kilns and the Cu Lao Cham shipwreck [36,38], the Zr peak is systematically more intense in Vietnamese productions (compare Figure 3 (Jingdezhen sherds) and Figure 4 (Vietnam sherds)). Titanium content, and particularly the Ti/Fe ratio, has also been identified as an effective criterion for distinguishing between different raw materials [90]. Comparison of Figures 3 and 4 further reveals a high Ti level in the bodies of the Vietnamese samples stylistically related to ceramics from the Cu Lao Cham shipwreck.

Although the decorative motifs of the TL1 and TL2 sherds are visually very similar (Table 1), comparison of the relative intensities of the Rb and Zr peaks, together with the relative Ti/Fe peak intensity (Figure 5), indicates that the SD (TL1) sherd is compositionally closer to Vietnamese porcelains from the Chu Đau kilns. In contrast, the

GD (TL2) sherd, characterized by a strong Rb signal, corresponds well to the compositional features observed for Jingdezhen porcelains (Figure 2). However, stylistically, the GD (TL2) sherd look Vietnamese. While visual comparison may be effective in some clear-cut cases, quantitative analysis based on fitted spectra and comparison of characteristic peak areas become necessary when the differences are more subtle.

As shown by the Si-K-Ca (Figure 6), Sr-Y-Rb, and Sr-Zr-Rb (Figure 7) ternary diagrams, constructed from peak areas calculated using Artax software, the artifacts can be classified into distinct groups based on both body and glaze compositions.

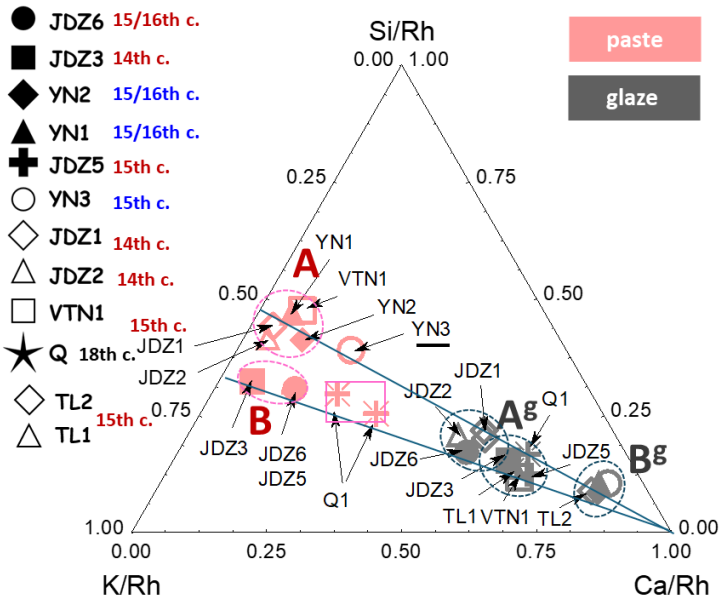


Figure 6. Ternary diagrams constructed from XRF peak areas of Si, K, and Ca. Data were normalized using the Rh Kα peak.

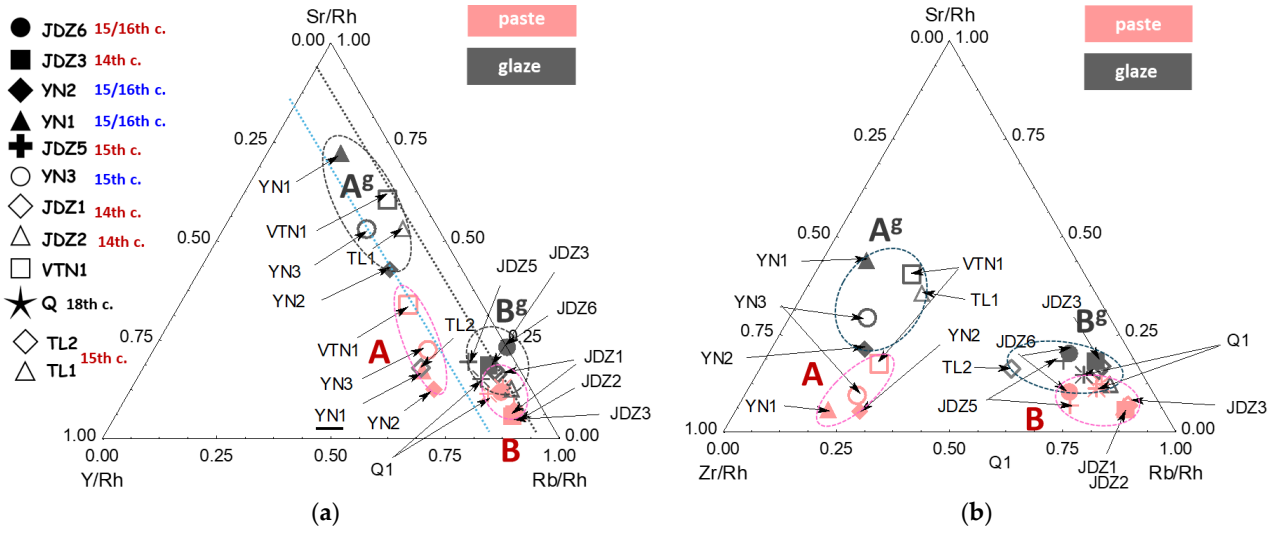


Figure 7. Ternary diagrams constructed from XRF peak areas of the following elements: Sr, Y, and Rb (**a**), and Sr, Zr, and Rb (**b**). Data were normalized using the Rh Kα peak.

Based on the Si-K-Ca diagram, two main groups (A and B) are identified for the ceramic bodies by comparing the potassium signal with those of silicon and calcium. Group B includes JDZ3 (Jingdezhen, mid-14th century; Table 1), JDZ5 (Jingdezhen, 15th–16th century), and JDZ6 (Jingdezhen, 15th–16th century) whereas Group A comprises JDZ1 (white ware, 14th century), JDZ2 (white ware, 14th century), YN1, YN2, and YN3 (15th–16th

century, assigned to Yunnan kilns), as well as VTN1 (assigned to Vietnam, 15th century). A third group, characterized by a higher calcium contribution, corresponds to a Qing dynasty sherd (sample Q).

Quantitative comparison of peak areas permits more refined categorization.

In the Sr-Y-Rb diagram (Figure 7), only two groups of ceramic bodies can be distinguished, although they are relatively close to each other. Group A includes YN1, YN2, and YN3 (all stylistically assigned to Yunnan kilns), as well as GD (TL2), whereas Group B consists of JDZ1, JDZ2, and JDZ3 as well as the Q sample (all from Jingdezhen). These results confirm that the relative intensities of the Rb, Sr, Y, and Zr signals provide a reliable fingerprint of raw material sources. Replacing yttrium with zirconium in the ternary plots enhances the distinction between the Yunnan sherds (YN1, YN2) and those assigned to Jingdezhen (JDZ1, JDZ2, JDZ3, JDZ5, and JDZ6), consistent with the higher zirconium content observed in Vietnamese artifacts probably produced using sands from the Hong River basin [36–38]. In this case, the classification derived from XRF peak areas is in good agreement with the visual assignments and archaeological contexts.

Figures 6 and 7 further demonstrate that this ternary diagram clustering approach is also effective when applied to glaze compositions. In the Si-K-Ca diagram, two well-defined groups are observed. Group B^g comprises YN1, YN2, and YN3, all from Yunnan, together with VTN1 (assigned to Vietnam) and TL1 assigned stylistically to Vietnam; whereas Group A^g, includes JDZ1, JDZ2, JDZ3, JDZ5, JDZ6, and Q, all assigned to Jingdezhen. This indicates that glaze recipes were relatively specific to the different production regions. For both Yunnan and Vietnamese kiln productions, the Hong River basin and its associated riverine sediments may have provided a common source of raw materials. These classifications again agree well with the assignments based on archaeological contexts and visual examination.

Replacing yttrium with zirconium yields similar results, although with slightly greater heterogeneity, clearly distinguishing Yunnan and Vietnamese porcelains (Group A) from those produced at Jingdezhen (Group B). A slight difference is observed between the Yunnan and Vietnamese (VTN1) sherds; however, this variation is of the same order as the compositional heterogeneity observed among sherds from a single kiln. Further studies based on a larger corpus are required to establish robust criteria for distinguishing these productions.

The glaze of SD (TL1) is very close to that of VTN1 (assigned to Vietnam; Table 1), whereas GD (TL2) is close to, but distinct from, the Jingdezhen Group B. Thus, despite their similar stylistic features, the TL1 and TL2 sherds appear to have been produced using raw materials from different sources.

3.2. Blue Decoration and Sources of Cobalt

We now examine the information derived from XRF analyses of blue-decorated glazes. Figure 8 illustrates the distribution of peak areas for cobalt and geologically associated elements, namely arsenic, iron, manganese, nickel, bismuth, and titanium. Significant arsenic contents in cobalt sources have been reported for ores used China during the Yuan dynasty, when cobalt ores were imported from the western borders of the Yuan Empire, including Persia [7,8], as well as during the Qing Dynasty, when smalt was imported from Europe [28–34]. In contrast, elevated iron and manganese contents are characteristic of Asian cobalt sources used during the early and late Ming dynasty, respectively [1,7,8,14,17,24].

Differences observed between measurements performed on the same sherd (e.g., JDZ3 and VTN1) provide an estimate of intrinsic sample heterogeneity combined with measurement uncertainty [78,80] and/or may reflect the heterogeneous mixing of ores from differ-

ent mining locations [18,30,85,88,89]. However, the Co-As-Mn, Co-Fe-Mn, and Fe-As-Mn ternary diagrams clearly distinguish four compositional groups:

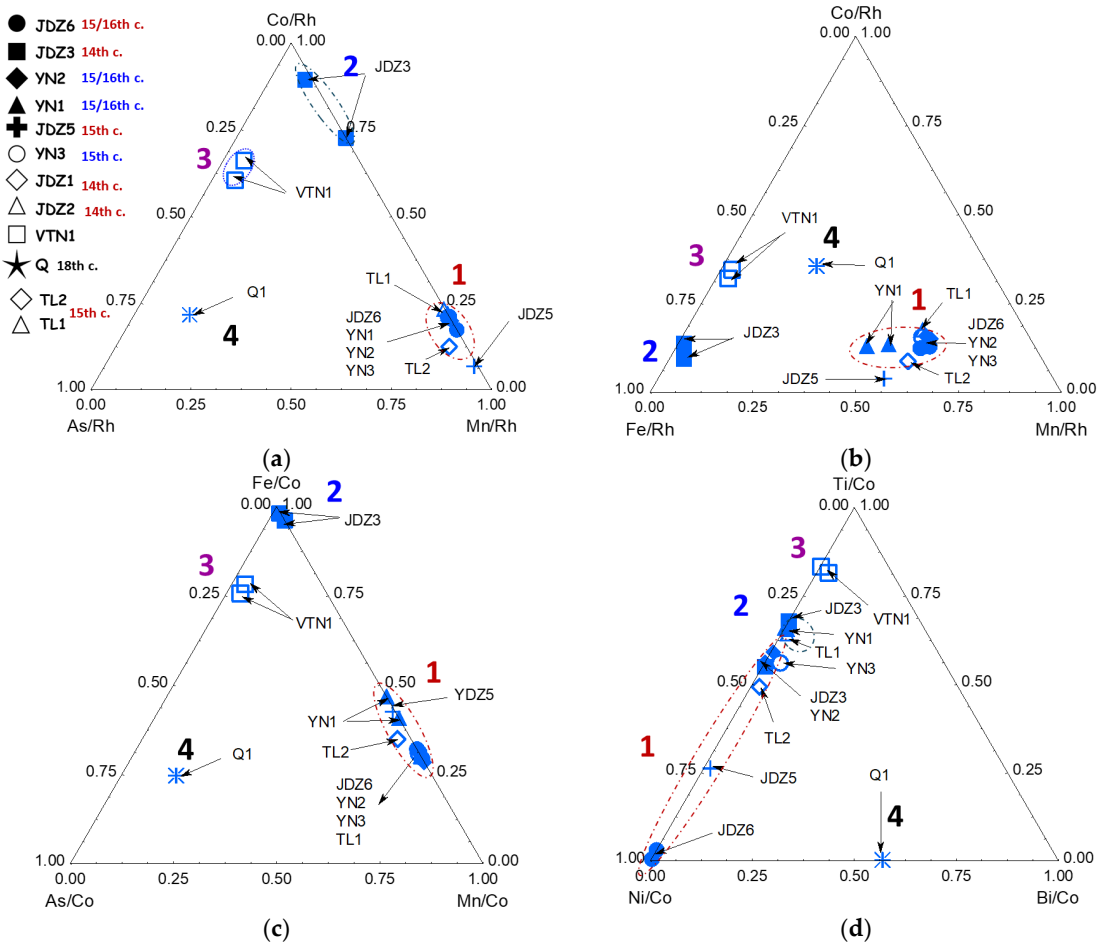


Figure 8. Classification of glaze compositions based on characteristic XRF signals of cobalt and elements commonly associated with cobalt ores: As (**a**,**c**), Fe (**b**,**c**), Mn (**a**,**b**), Ni (**d**), Ti (**d**), and Bi (**d**) (see Table 1). Q corresponds to a Qing dynasty sherd (Qianlong reign) partially decorated using smalt. Multiple measurement points were analyzed for selected sherds.

(i) Group 1: Sherds JDZ6 (Jingdezhen, 15th–16th century), YN1 (Yunnan, 15th–16th century), YN2 (Yunnan, 15th–16th century), and YN3 (Yunnan, 15th century) cluster together and are closely related to JDZ5 (Jingdezhen, 15th–16th century). All are characterized by high manganese contents. Considering the Ti and Ni signals further subdivides Group 1 into two subgroups, one comprising JDZ6 and the other comprising the remaining sherds. Their common feature appears to be their period of production.

(ii) Group 2: JDZ3 (Jingdezhen, mid-14th century).

(iii) Group 3: VTN1 (assigned to Vietnam, 15th century) form two distinct groups, both characterized by low manganese and high iron contents. Measurable arsenic is also present in the blue glaze of VTN1.

(iv) Group 4: The blue decoration of sample Q is rich in arsenic and contains detectable traces of bismuth, an element characteristic of some European cobalt sources [18,30,85].

These results suggest that cobalt sources are differentiated primarily according to chronological period rather than production site. This pattern may be explained by the limited number of geological sources suitable for cobalt exploitation and the long-distance trade of cobalt ores and pigments. The use of similar cobalt materials at kilns located in different regions of Asia is therefore unsurprising. Long-distance trade involving cobalt

sources outside the Chinese cultural sphere has been well documented since the Yuan dynasty [5–8,12,18,85], and cobalt materials were subsequently distributed over considerable distances and used in multiple production centers.

The nickel signal further discriminates manganese-rich cobalt sources into subgroups. SD (TL1) and GD (TL2) exhibit similar cobalt-related compositional characteristics, which are consistent with their similar production periods and graphic styles. However, their broader elemental signatures indicate different raw material sources: SD (TL1) is compositionally closer to the Vietnamese VTN1 sherd, whereas GD (TL2) is closer to the Jingdezhen group. This discrepancy between stylistic similarity and compositional affinity raises the possibility of technological transfer, imitation, or the circulation of Jingdezhen products in Vietnam and warrants further investigation.

3.3. Body and Glaze 'Raman' Analysis

While comparison of raw-material-related XRF signals is effective for classifying bodies, glazes, and blue-decorated areas, complementary information can be obtained from optical spectroscopy (Figures 9–12).

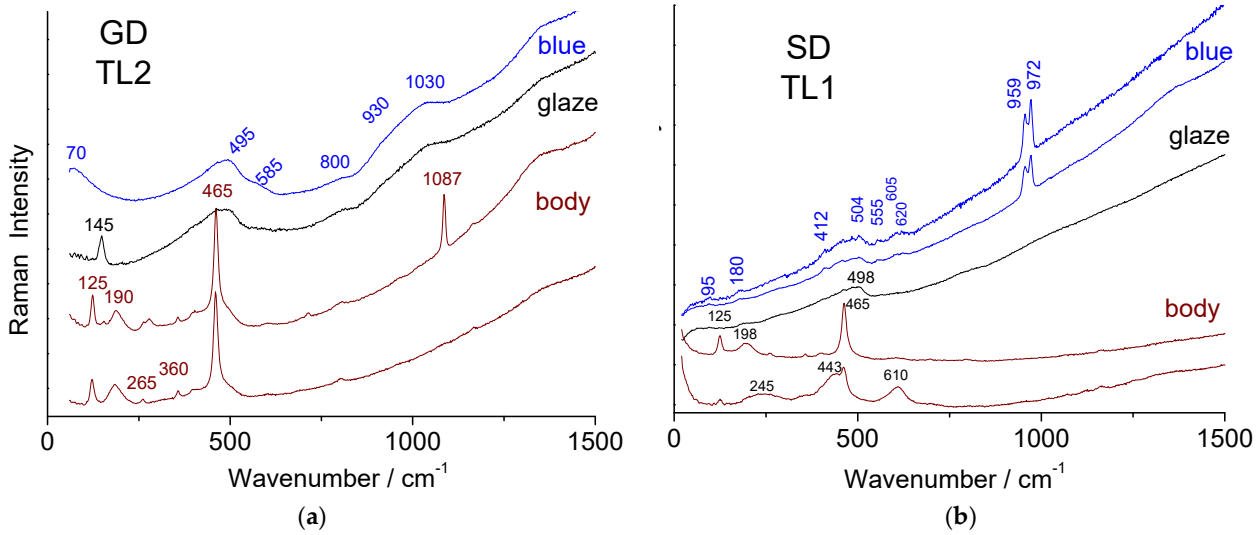


Figure 9. Representative Raman spectra obtained from the GD TL2 (**a**) and SD TL1 (**b**) sherds using 514.5 nm excitation.

A Raman spectrum consists of the Raman signal *stricto sensu* (stretching, bending, liberational, translational, and lattice vibrational modes of crystalline and amorphous phases) [59] and a fluorescence component arising from the bulk material (defects and traces of transition metals and rare-earths elements [60–62,91,92]) or from species adsorbed within porosity or on the surface (often bio-organic residues related to burial). This fluorescence contribution is often referred to as a "background" and is frequently disregarded and even subtracted, despite the valuable information it may contain.

3.3.1. Fundamental Raman Vibrational Signatures

Body and Colorless Glaze

We will first consider the vibrational signatures recorded on fracture surfaces of the ceramic bodies (Figures 9 and 10). In most cases, Raman spectra of hard-paste porcelain bodies are very similar and show either:

(i) Spectra dominated by quartz grains, identified by the intense SiO_4 tetrahedral deformation mode at ~465 cm^{-1} [93–97] (sometimes shifted to 460 or 462 cm^{-1} due to ten-

sile stress induced by the surrounding amorphous matrix [95,96]), along with other characteristic quartz peaks at ~125 and ~200 cm^{-1};

(ii) Spectra corresponding to the amorphous phase (a good example is the (blue) glaze spectrum in Figure 9a) and/or mullite (good examples are the spectra in Figures 9b and 10d).

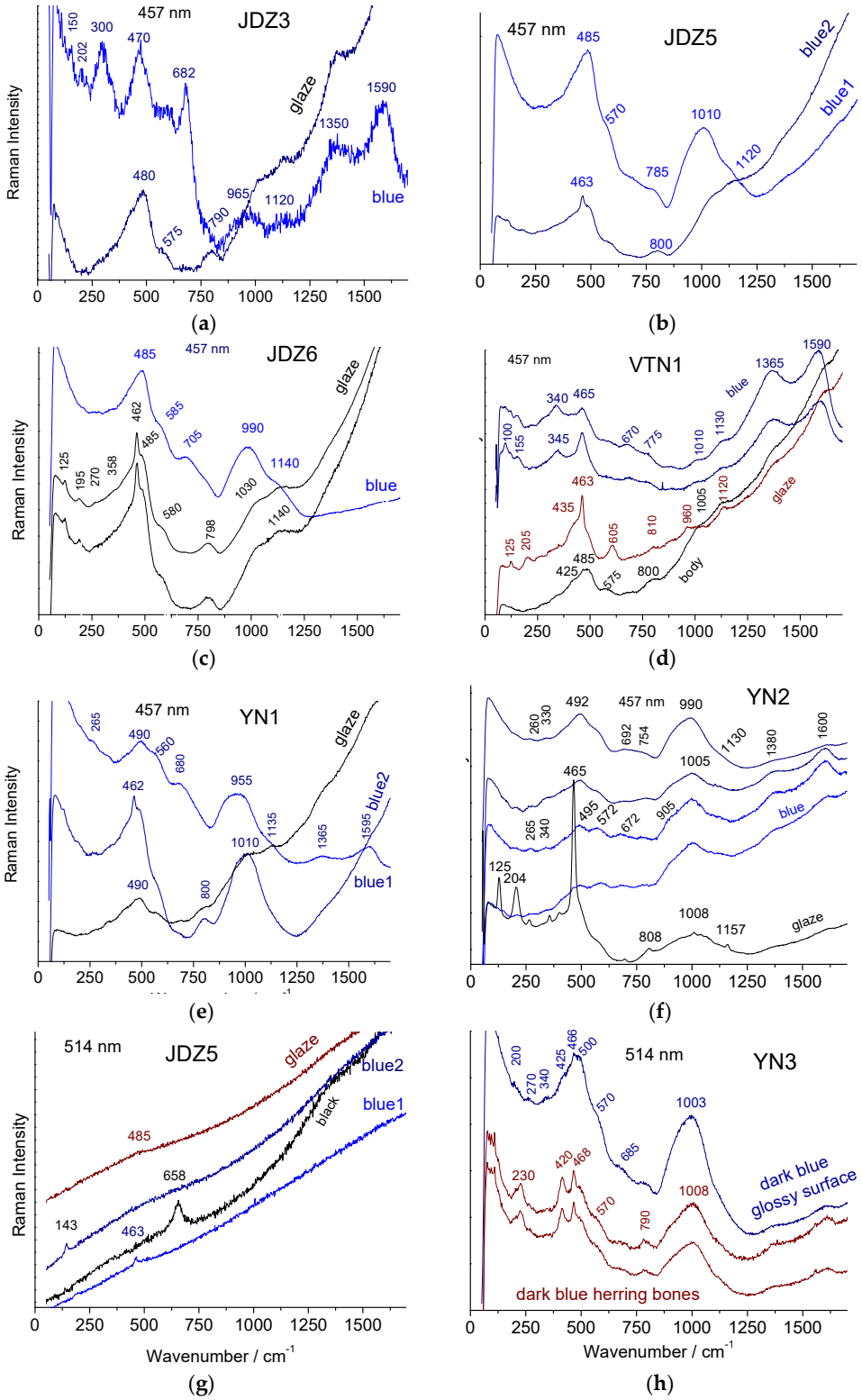


Figure 10. Representative Raman spectra recorded on blue and colorless glazed zones of JDZ3, JDZ5, JDZ6, YN1, YN2, YN3, and VTN1 sherds using blue (**a**–**f**) or green laser (**g**,**h**) line.

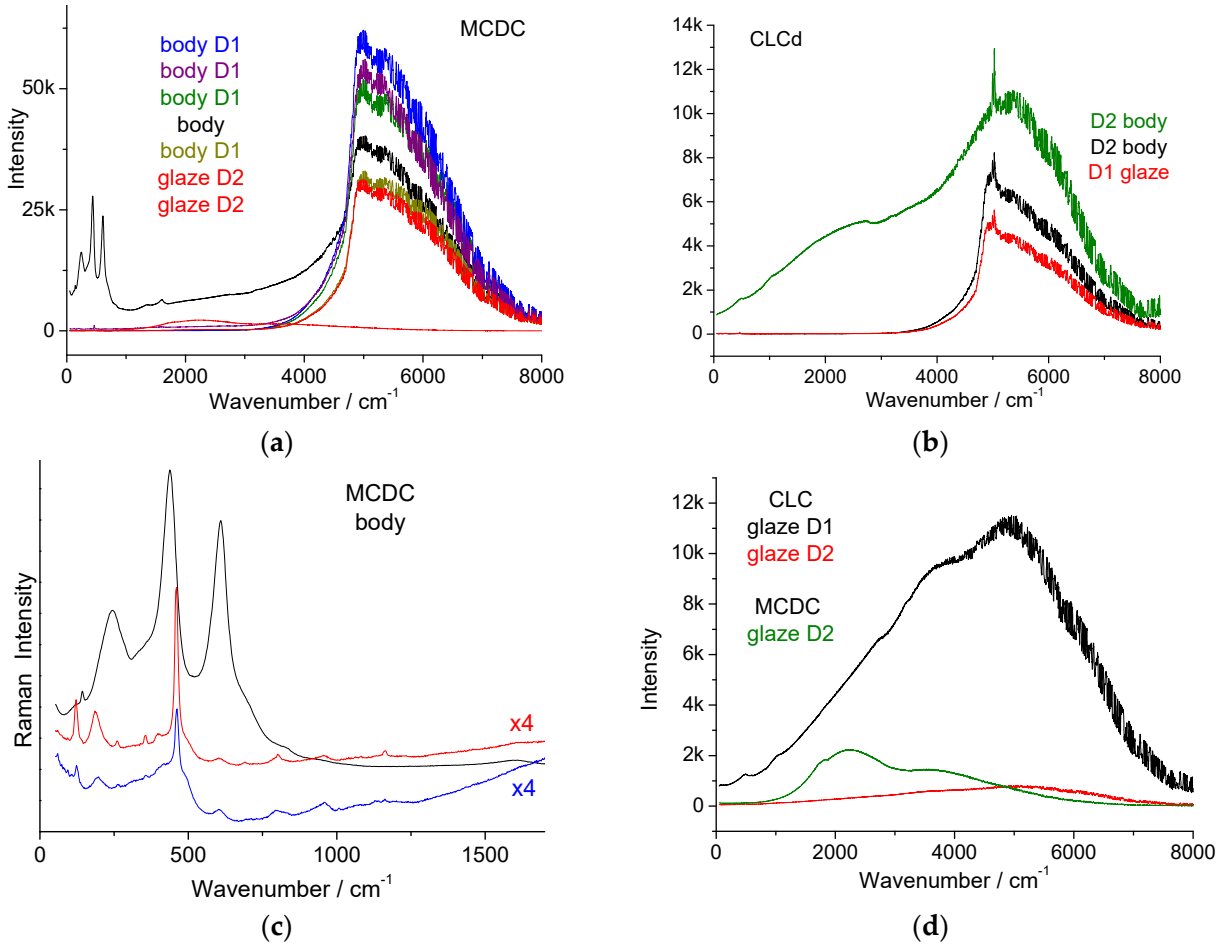


Figure 11. Examples of fluorescence spectra recorded on polished sections of the body and on glaze surfaces of blue-and-white porcelain sherds and from Chu Dau (MCDC) kiln excavations (**a**,**c**) and from the Cu Lao Cham (CLC) shipwreck (**b**,**d**), previously analyzed in ref [36].

The spectra of these two latter phases (the glassy phase in-between mullite needles forming the porcelain body) are difficult to distinguish, as their spectra are generally weak and composed of broad bands [95,96,98–101], due to the poor covalence of Al-O bonds. Excitation with a blue or violet laser is often required to obtain spectra of sufficient quality. These spectra typically consist of a broad, asymmetric band centered around ~485 cm^{-1}, with additional components near ~575 and ~800 cm^{-1}. The presence of mullite is indicated by a more clearly defined band around ~960 cm^{-1} [100–106].

Signatures of the TiO_2 polymorphs, anatase (main peak at 144 cm^{-1}) or rutile (broad triplet around ~250–450 and at 610 cm^{-1} [102]) are frequently observed but are not considered diagnostic. In rare cases, specific residual phases such as calcite (1085 cm^{-1} narrow peak [103]), silicates (alpha or beta wollastonite, with a sharp peak around 975 or 995 cm^{-1} [104,105]), or calcium phosphates (main peak near ~965 cm^{-1} [106–109]) are detected. Cristobalite is only rarely observed [107]. Among the sherds analyzed here, only the GD (TL2) sherd exhibits Raman features characteristic of calcite, with a band at 1085 cm^{-1}, whereas the SD (TL1) sherd displays a 969–972 cm^{-1} doublet indicative of calcium silicate(s) and/or calcium phosphate] (Figure 8), consistent with phosphatic glaze compositions. Such features are commonly observed in English bone china and French soft-paste porcelains [81,95,107–109], but have occasionally been reported in certain Chinese glazes due to the addition of ashes or bones to the glaze [2,29,110,111].

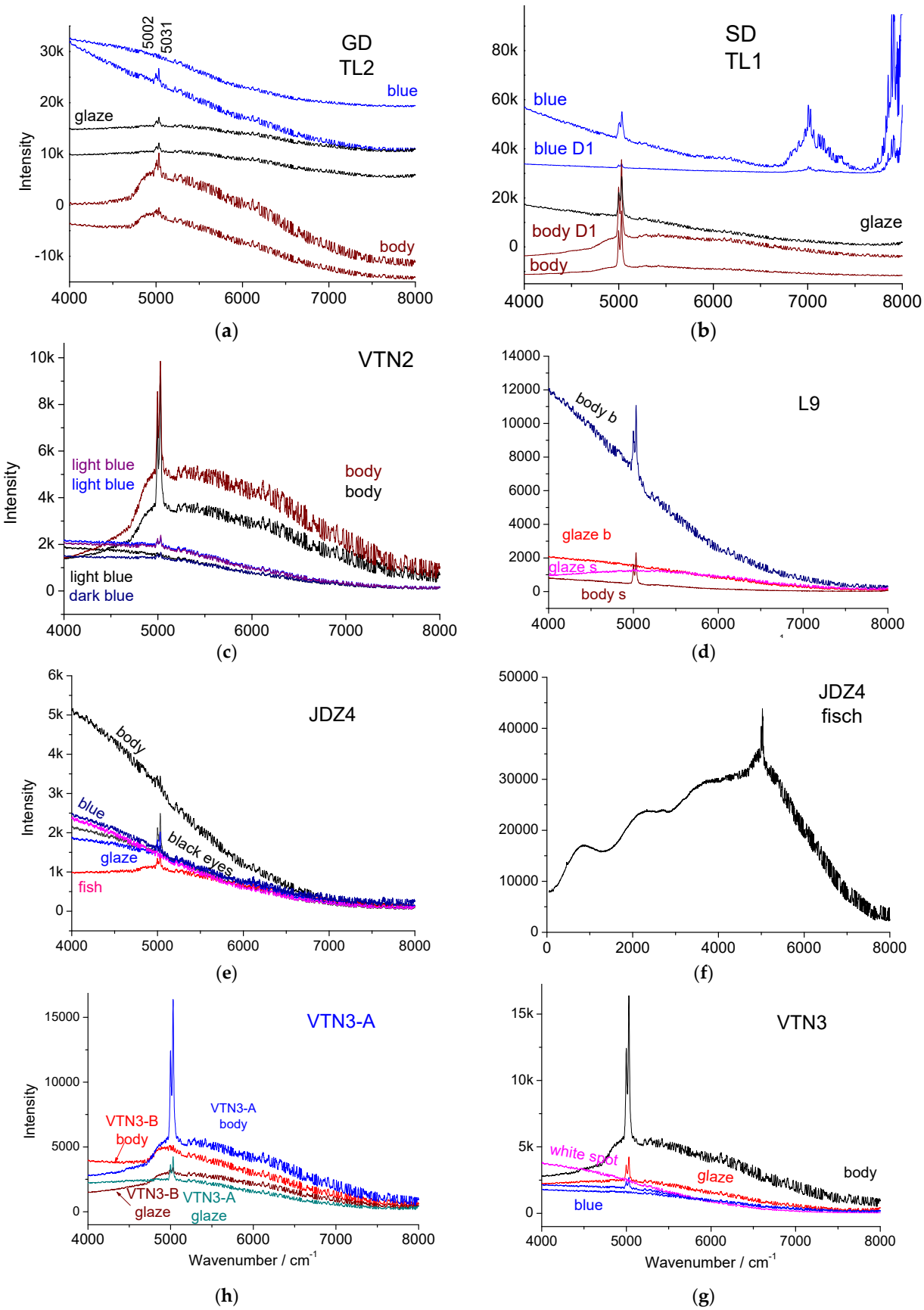


Figure 12. Fluorescence spectra recorded with 514.5 nm excitation on the body and glaze of GD (TL2) (**a**), SD (TL1) (**b**), VTN2 (**c**), L9 (**d**), JDZ4 (**e**,**f**), VTN3-A (h) and VTN3-B (g) sherds. Some spectra were recorded using an optical density filter (D1: 10%).

Previous studies have shown that the shape of the SiO_4 stretching massif, as well as the ratio between the peak area of deformation and stretching modes, can be used to classify glazes according to the degree of polymerization of the silicate network, effectively reflecting firing temperature, provided that the spectra are of sufficient quality [112–114]. In this respect, the stretching signatures of the TL2 and TL1 glazes are markedly different. Raman spectroscopy is therefore as discriminating as pXRF in this case. The broad 930–1030 cm^{-1} doublet observed for the TL2 sherd corresponds to a 'standard' porcelain glaze, whereas the narrow doublet recorded for the TL1 glaze is exceptional.

Figure 9 illustrates variations in the SiO_4 stretching band profiles for other glazes. The maximum wavenumber of the principal component ranges from ~990 to ~1025 cm^{-1}, reflecting substantial differences in glaze composition and firing temperature [112]; glazes with lower wavenumber maxima are associated with lower firing temperatures. Spectra obtained from blue-decorated glazes are generally of higher quality due to the absorption of red fluorescence by the blue pigment.

Since blue coloration results from Co^{2+} ions dissolved within the silicate network rather than from the formation of a distinct crystalline phase, no additional Raman bands attributable to cobalt compounds are observed [5].

In some blue-glazed areas (Figure 10), localized dark defects visible under optical microscopy show dendritic crystallization and yield Raman spectra characterized by bands near ~240, ~440, ~690, and ~1350 cm^{-1}, consistent with the ε-Fe_2O_3 (epsilon hematite) phase. This phase has been frequently present in Vietnamese [37], Japanese [115,116], and Chinese [117–122] porcelain glazes.

Quantitative differentiation based on Raman spectroscopy is only effective when glazes differ significantly in composition and firing temperature. For example, the main SiO_4 stretching component of JDZ6 (Jingdezhen) and YN2 (Yunnan) glazes peak near ~990 cm^{-1}, whereas those of JDZ3 and JDZ5 (Jingdezhen) and YN3 (Yunnan) peak at higher wavenumbers (1000–1025 cm^{-1}). However, the strong fluorescence background often requires baseline subtraction to determine peak positions accurately, increasing uncertainty. Consequently, these differences alone are insufficient for reliable kiln attribution.

Figure 11, recorded over a very wide spectral range, highlights the importance of the so-called "continuous fluorescence background", which is often neglected and removed in many Raman studies. Luminescence emission generally consists of both broad bands and narrow components, depending on the physical origin of the emission and the structural environment hosting the emitting defects. Briefly, narrow components arise from electronic transitions excited by the laser source in ions with partially filled 3d (transition metals) or 4f electron shells (rare earth elements) [60–62]. The narrow peak transitions, which are exploited in applications such as laser sources [123] and mechanical stress probes [124–127], are much better documented than those responsible for broad emission bands.

3.3.2. Fluorescence Signatures

We consider here the fluorescence intrinsic to the ceramic material, which is stable under laser irradiation, rather than the fluorescence that originates from films of organic or biological contaminants that develop on the surface of the sherds buried in the ground. This extrinsic fluorescence can be decreased/eliminated within a few minutes by strong laser irradiation (>2 $mW/\mu m^2$ for a green laser, and at lower power for a blue laser).

In particular, the narrow doublet at 5020–5037 cm^{-1} (corresponding to 692–694 nm for 514.5 nm excitation) is attributed to Cr^{3+} ions incorporated into an α-alumina matrix with corundum structure [124,126,127]. The broad features similar to those observed on either side of this doublet are generally associated with Cr^{3+} ions hosted in

disordered structures such as a transition alumina matrix, especially γ-alumina with a spinel-type structure [127].

During firing, kaolinite decomposes into metakaolin at approximately 600 °C [128] and subsequently reacts with alkali and alkaline-earth fluxes between 800 and 900 °C to form a disordered aluminosilicate phase with a spinel-type structure around 900–1000 °C [128–134]. This phase evolves above 1100 °C into 2:1 mullite with a squared morphology, which further transforms above 1200–1250 °C into acicular 3:2 mullite, depending on reaction kinetics and firing duration [131–134]:

$$2\ [2\ Al_2O_3\ SiO_2] \Rightarrow [3\ Al_2O_3\ 2\ SiO_2] + [Al_2O_3] \quad (1)$$

The relative intensity of the narrow doublet compared to the broad fluorescence component is therefore directly related to the amount of alumina produced during the transformation of 2:1 mullite into 3:2 mullite, a process driven by firing temperature and duration.

Figure 12 compares fluorescence spectra in the 4000–8000 cm^{-1} range (relative Raman shift for 514.5 nm excitation, corresponding to 650–800 nm in absolute wavelength) for different sherds. The intensity of the 5002–5035 cm^{-1} Cr^{3+} doublet (i.e., 692.8 and 694.4 nm) varies significantly depending on both the sherd and the analyzed zone (body or glaze). The very broad band below is assigned to chromium luminescence in disordered (transition alumina) and glassy phases [13]. According to Eq. (1), higher doublet intensity reflects a greater abundance of 3:2 mullite and likely a higher firing temperature. The strongest signals are observed for VTN3 (stylistically attributed to the Cu Lao Cham shipwreck; production attributed to Chu Dau, Hai Duong Province, Vietnam), VTN2, and SD (TL1), indicating high mullite contents and firing temperatures exceeding 1250 °C. In contrast, the spectra obtained from the TL2 sherd, decorated with a bird-foot motif, are markedly different, suggesting that it may originate from a different production tradition and supporting the Raman and XRF results. The TL2 (Vietnam) and JDZ4 (Jingdezhen, underglaze decoration) sherds exhibit weak or absent doublets, indicating firing temperatures below 1200 °C.

3.4. Comparison with PCA and Hierarchical Clustering Analysis

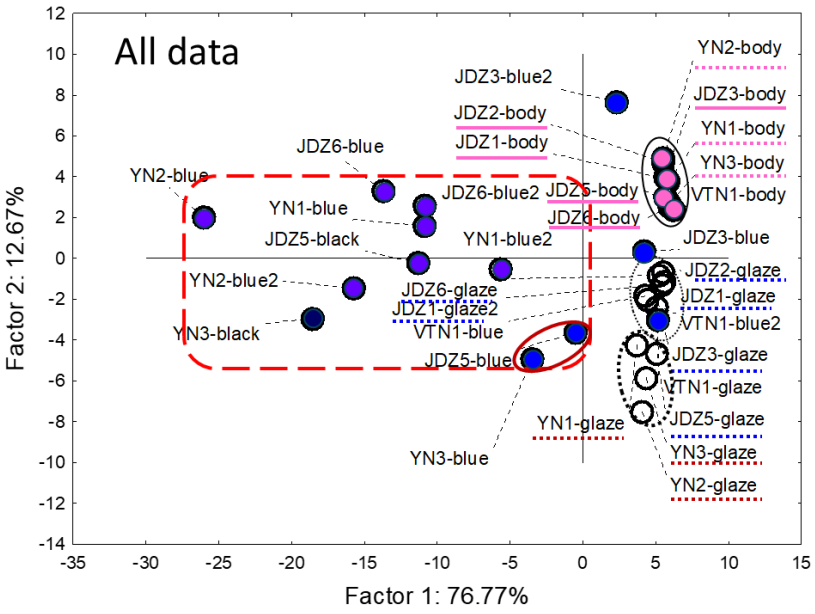
A comparison between the elemental composition characteristics and the identified phases was carried out using a reasoned approach, based on microstructural data. By contrast, many studies rely on algorithmic methods such as Principal Component Analysis (PCA), applied to elemental composition data alone.

Examination of the PCA plot in Figure 12 shows a clear separation between the data obtained from the bodies and those from colorless glazes or cobalt blue-colored glazes. In particular, the blue-glazed analyses of sherds JDZ3, VTN1, JDZ5, and YN3 are clearly distinguished from the others. It should be recalled that JDZ3 corresponds to a mid-14th century production from Jingdezhen; VTN1 is a sherd found in Java and potentially of Vietnamese origin and assigned to the 15th century; JDZ5 originates from 15th–16th century Jingdezhen; and YN3 is attributed to Yunnan (15th century). Their production dates are rather similar.

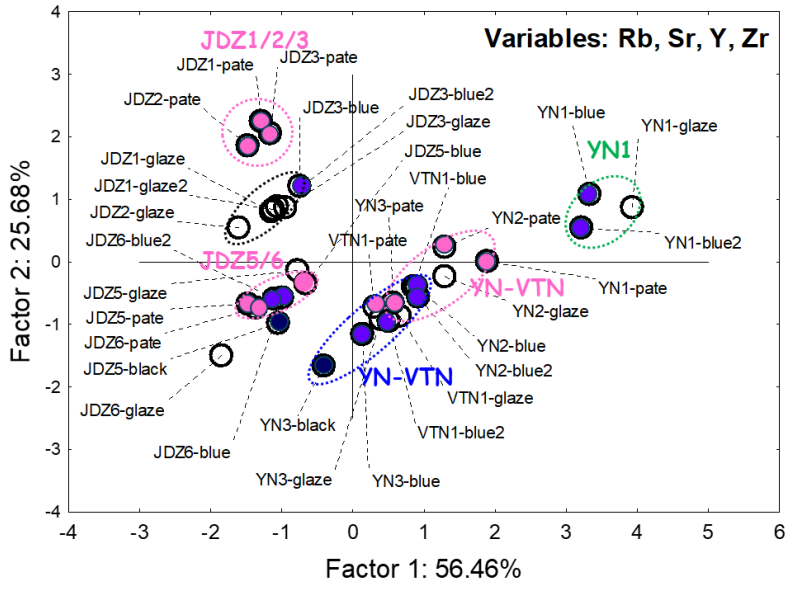
However, as observed for the ternary diagrams constructed from all elemental signals, this classification remains partial and, in some cases, does not correspond to the attributions based on visual criteria and proposed production origins.

PCA calculated using Rb, Sr, Y, and Zr impurities as variables is presented in Figure 13b; the classifications become more efficient when irrelevant elements are excluded, as the 'noise' induced by non-discriminant elements is reduced. For instance, the score plot calculated using all data (Figure 13a) first categorizes the different parts studied: body, colorless glaze, and blue glaze. However, the blue glazes of JDZ3 and VTN3 fall out-

side their corresponding main groups. On the other hand, the score plot calculated using impurities that produce relatively strong XRF peaks (Figure 13b) allows a clearer separation of ceramic bodies from the Jingdezhen kilns and those originating from Yunnan or attributed to Vietnam. JDZ5 and JDZ6 form a specific group, as does YN1 sherd. For the Jingdezhen sherds, the distinction between paste and glaze is also effectively achieved.



(**a**)



(**b**)

Figure 13. PCA score plots using first and second factors calculated with all elemental composition data (**a**) and using only impurity elements (**b**) as variables. See Table 1 for details. The lines approximately determine the groups.

Ternary diagrams constructed from selected elemental signals (Figures 6 and 7) appear to be more discriminating, and the direct visualization of compositional relationships within a ternary system gives useful information: in particular, separation between sherds assigned to Yunnan and Vietnam is more effective.

Hierarchical clustering using Euclidean distance and Ward's method yields comparable results. Figure 14 shows two examples of hierarchical classifications: (a) calculated

using the Rb, Sr, Y, and Zr signals normalized to Rh for body and glaze analyses, and (b) calculated using the As/Co, Mn/Co, Fe/Co, Bi/Co, and Ni/Co ratios for blue-glazed areas.

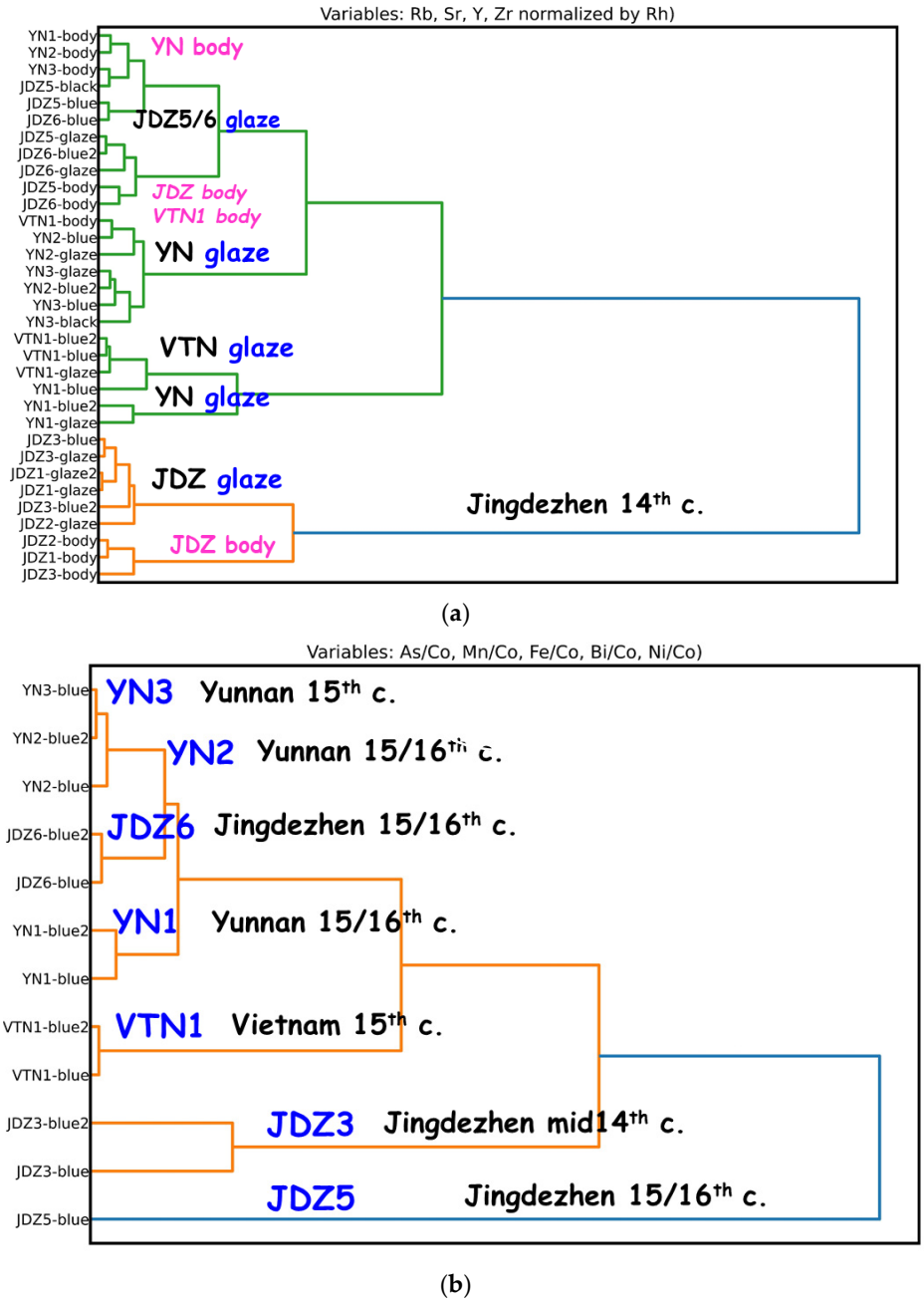


Figure 14. Ward's hierarchical clustering diagrams calculated from XRF signals of impurity elements (**a**) and cobalt-associated elements (**b**).

In the first dendrogram (Figure 14a), the first categorization depends on the type of material (body or glaze), and part of the Jingdezhen production is distinguished; however, sherd JDZ5 and JDZ6 (Jingdezhen, 15th–16th century) cluster with samples from Yunnan and Vietnam dating to about the same period. Supplementary Materials (Table S1) For blue glaze, the categorization depends on the period.

Overall, PCA and Euclidean clustering techniques operate in a multivariate hyperspace and allow classification without incorporating prior knowledge of the geological origin of the raw materials used in ceramic production. A comparison with classifications obtained through a reasoned interpretation of compositional diagrams demonstrates that

the latter approach is at least as effective, and in some cases more effective, than purely algorithmic ("blind") statistical methods.

4. Conclusions

The primary objective of the pXRF measurements was to validate a rapid characterization procedure applicable not only to sherds but, more importantly, to intact objects—specifically 'white' or blue-and-white decorated porcelains, where signals from impurities in sands and fluxes, as well as transition metals associated with cobalt, serve as effective markers for categorization. However, for other types of ceramics, where heavy element content (Sn, Sb, Ba, etc.) might otherwise serve as a distinguishing factor, pXRF analysis is compromised by variations in glaze thickness. This study confirms the effectiveness of comparing XRF signals of impurities associated with sands (Y, Zr), calcium sources (Sr), and potassium sources (Rb) for identifying ceramics produced using the same or similar raw materials (summarized in Table 1). This approach proves more discriminating than comparisons based on major elemental compositions, likely due to the coexistence of multiple manufacturing recipes within a single workshop and the 'noise' introduced by elements whose variations are not discriminatory. The comparison of cobalt-related signals and associated elements, reflecting ore provenance, geological context, and purification processes that vary over time, is also shown to be highly effective. The use of iron-rich cobalt in Jingdezhen during the 14th century, followed by manganese-rich cobalt from the 15th to the late 17th century, is confirmed. Additional information is provided by the XRF signals of titanium, nickel, and bismuth. As expected, the use of smalt is associated with elevated arsenic and bismuth contents, and, for Qing dynasty productions, the Ni/Ti ratio further distinguishes technological choices. We show that algorithmic techniques such as PCA and Euclidean clustering lead to similar classifications, but are less efficient than the reasoned approach.

Although Raman spectroscopy does not provide a classification as discriminating as impurity-based XRF analysis, it enables the identification of specific phases associated with particular technological practices and thus represents a valuable complementary tool. This work demonstrates, for the first time, the importance of analyzing the fluorescence 'background', often not considered in Raman studies (or even eliminated by subtraction of the so-called 'background'), as the chromium fluorescence doublet provides a quantitative indicator of the amount of 3:2 mullite formed from 2:1 mullite and, consequently, of the firing temperature.

While the limited number of sherds restricts the statistical strength of the conclusions, the results are consistent with the published literature. The JDZ3 sherd (Jingdezhen, stylistically attributed to the mid-14th century) and the VTN1 sherd (attributed to the 15th century) are characterized by iron-rich cobalt, consistent with early Ming production. Although the production site of VTN1 cannot be securely assigned, it shows chemical affinities with both Yunnan and Vietnamese ceramics, whereas its decorative style, ceramic texture, and body density shows closer affinities to Vietnamese wares.

Sherds decorated using manganese-rich cobalt correspond to later periods. TL1 and TL2 belong to the same group with regard to their cobalt characteristics, consistent with production during the same period. However, the SD sherd is similar to the VTN1 sherd, which is considered to be of Vietnamese origin, whereas the TL2 sherd shows a very high similarity of its glaze with Jingdezhen productions. TL1, with its five-clawed dragon motif [55], may have been probably produced at the imperial kiln complex at the Thang Long site. The production origin of TL2, however, remains open: its ceramic texture differs from typical Jingdezhen porcelain, while its bird-foot motif finds parallels among Vietnamese wares associated with the Hoi An shipwreck. Taken together, these results support

a Vietnamese origin for TL1, with a possible connection to the Thang Long imperial kiln, whereas TL2 may represent a different Vietnamese production tradition despite the compositional affinity of its glaze with Jingdezhen wares. Its parallels with ceramics from the Hoi An shipwreck further suggest a possible connection with Chu Đau or, more broadly, another Vietnamese production center. More shards are required to go further in the assignment of the place of production. Finally, the strong similarity between Yunnan and Vietnamese blue-and-white productions of the fifteenth to sixteenth centuries is confirmed, particularly their high zirconium contents, while rubidium levels provide a reliable criterion for distinguishing between them.

Supplementary Materials: The following supporting information can be downloaded at https://www.mdpi.com/article/10.3390/heritage9090362/s1.

Author Contributions: Conceptualization, P.C. and C.-F.S.; methodology, P.C. and G.S.-F.; investigation, P.C.; data curation, P.C. and G.S.-F.; writing—original draft preparation, P.C., G.S.-F. and C.-F.S.; writing—review and editing, P.C., G.S.-F., C.-W.C., H.-C.H. and C.-F.S.; visualization, P.C. and G.S.-F. All authors have read and agreed to the published version of the manuscript.

Funding: This research received no external funding.

Data Availability Statement: All data included in the article and Supplementary Materials.

Conflicts of Interest: The authors declare no conflicts of interest.

References

1. Zhang, F. The origin and development of traditional Chinese glazes and decorative ceramic colors. In *Ancient Technology to Modern Science*; Kingery, W.D., Ed.; Ceramics and Civilization Series, Vol. 1; The American Ceramic Society: Colombus, NA, USA, 1985; Volume 1, pp. 163–180.
2. Guo, Y. Raw materials for making porcelain and the characteristics of porcelain wares in North and South China in ancient times. *Archaeometry* **1987**, *29*, 3–19. [CrossRef]
3. Yap, C.T.; Hua, Y. Raw materials for making Jingdezhen porcelain from the Five dynasties to the Qing dynasty. *Appl. Spectrosc.* **1992**, *46*, 1488–1494. [CrossRef]
4. Wood, N. *Chinese Glazes: Their Origins, Chemistry, and Recreation*; University of Pennsylvania Press: Philadelphia, PA, USA, 1999.
5. Chen, Y.; Zhang, F.; Zhang, X.; Jiang, J.; Li, D. A study on Tang blue and white wares and sources of cobalt pigments used. In *Science and Technology of Ancient Ceramics 3*; Guo, J., Ed.; Shanghai Research Society of Science and Technology of Ancient Ceramics: Shanghai, China, 1995; pp. 204–210.
6. Yu, K.N.; Miao, J.M. Non-destructive and quantitative investigation of Jingdezhen blue and white porcelains using EDXRF. *J. X-Ray Sci. Technol.* **1996**, *6*, 167–171. [CrossRef]
7. Wu, J.; Leung, P.L.; Li, J.Z.; Stokes, M.J.; Li, M.T. EDXRF studies on blue and white Chinese Jingdezhen porcelain samples from the Yuan, Ming and Qing dynasties. *X-Ray Spectrom.* **2000**, *29*, 239–244. [CrossRef]
8. Wen, R.; Wang, C.S.; Mao, Z.W.; Huang, Y.Y.; Pollard, A.M. The chemical composition of blue pigment on Chinese blue-and-white porcelain of the Yuan and Ming dynasties (AD 1271–1644). *Archaeometry* **2007**, *49*, 101–115. [CrossRef]
9. Wood, N.; Tite, M.S.; Doherty, C.; Gilmore, B. A technological examination of ninth-tenth century AD Abbasid blue-and-white ware from Iraq, and its comparison with eighth century AD Chinese blue-and-white sancai ware. *Archaeometry* **2007**, *40*, 665–684. [CrossRef]
10. Juan, W.; Leung, P.L.; Jiazhi, L. A study of the composition of Chinese blue and white porcelain. *Stud. Conserv.* **2007**, *52*, 188–198. [CrossRef]
11. Du, F.; Su, B. Further study of sources of the imported cobalt-blue pigment used on Jingdezhen porcelain from late 13 to early 15 centuries. *Sci. China Ser. E Technol. Sci.* **2008**, *51*, 249–259. [CrossRef]
12. Zhu, T.; Ding, X.; Kusimba, C.M.; Feng, Z. Using laser ablation inductively coupled plasma mass spectroscopy (LA-ICP-MS) to determine the provenance of the cobalt pigment of Qinghua porcelain from Jingdezhen in Yuan Dynasty of China (1271–1368AD). *Ceram. Int.* **2015**, *41*, 9878–9884. [CrossRef]
13. Bao, Z.; Yuan, H.; Wen, R.; Chen, K. The fast and direct characterization of blue-and-white porcelain glaze from Jingdezhen by laser ablation-inductively coupled plasma mass spectrometry. *Anal. Methods* **2015**, *7*, 5034–5040. [CrossRef]
14. Wang, W.; Zhu, J.; Jiang, J.; Xu, C.; Wu, S.; Guan, L.; Du, J. Microscopic analysis of "iron spot" on blue-and-white porcelain from Jingdezhen imperial kiln in early Ming dynasty (14th–15th century). *Microsc. Res. Tech.* **2016**, *79*, 1123–1130. [CrossRef]

15. Zhu, T.Q.; Zhang, Y.C.; Xiong, H.; Feng, Z.Y.; Li, Q.; Cao, B.L. Comparison of the Different Types of Qinghua Porcelain from Jingdezhen in the Yuan Dynasty of China (ad 1271–1368) by Micro X-ray Fluorescence Spectroscopy (μ-XRF) and Microscopy. *Archaeometry* **2016**, *58*, 966–978. [CrossRef]
16. Fischer, C.; Hsieh, E. Export Chinese blue-and-white porcelain: Compositional analysis and sourcing using non-invasive portable XRF and reflectance spectroscopy. *J. Archaeol. Sci.* **2017**, *80*, 14–26. [CrossRef]
17. Wen, J.; Chen, Z.; Zeng, Q.; Hu, L.; Wang, B.; Shi, J.; Zhang, G. Multi-micro analytical studies of blue-and-white porcelain (Ming dynasty) excavated from Shuangchuan island. *Ceram. Int.* **2019**, *45*, 13362–13368. [CrossRef]
18. Colomban, P.; Kirmizi, B.; Simsek Franci, G. Cobalt and associated impurities in blue (and green) glass, glaze and enamel: Relationships between raw materials, processing, composition, phases and international trade. *Minerals* **2021**, *11*, 633. [CrossRef]
19. Hoo, Q.; Wang, X.; Yuan, F.; Cao, X.; Cao, T.; Zhang, M. Microstructure and coloring mechanism of iron spots on bluish white porcelain from Jingdezhen of the Song Dynasty. *J. Eur. Ceram. Soc.* **2021**, *41*, 3816–3822. [CrossRef]
20. Li, Q.; Zhang, M.; Wang, L.; Yu, Y.; Xiong, L.; Zhou, J.; Yuan, F. Analyzing the formation mechanism of 'Huoshi-hong'characteristics in the blue-and-white porcelain of the Yuan Dynasty from Jingdezhen. *J. Eur. Ceram. Soc.* **2022**, *42*, 7360–7368. [CrossRef]
21. Xiong, L.; Yu, Y.; Li, J.; Wu, Q.; Wu, L.; Yuan, Y.; Li, D.; Li, Q. Analyzing the chemical compositions of Co-based materials in blue-and-white porcelains from the Yuan Dynasty. *Res. Sq.* **2023**. [CrossRef]
22. Li, J.; Yang, Y.; Zou, D.; Wu, L.; Wu, Q.; Lin, Z.; Li, Q. Recognition of Yuan blue and white porcelain produced in Jingdezhen based on graph anomaly detection combining portable X-ray fluorescence spectrometry. *Herit. Sci.* **2024**, *12*, 79. [CrossRef]
23. Zhang, R.; Gethin, P. Provenance of the cobalt pigment used for Jingdezhen minyao blue-and-white porcelain in the early Qing dynasty. *Ceram. Int.* **2021**, *47*, 25763–25768. [CrossRef]
24. Colomban, P.; Ngo, A.T.; Edwards, H.G.; Prinsloo, L.C.; Esterhuizen, L.V. Raman identification of the different glazing technologies of Blue-and-White Ming porcelains. *Ceram. Int.* **2022**, *48*, 1673–1681. [CrossRef]
25. Wu, T.; Wu, Q. Analysis of the Composition and Change of Chinese Blue and White Porcelain Pot Glaze from the Perspective of Archaeology. *Mediterr. Archaeol. Archaeom.* **2023**, *23*, 16–30.
26. Ma, Q.; Pollard, A.M.; Jiang, J.; Weng, Y. Evaluation of quantitative XRF analysis applied to determine cobalt sources in Chinese Blue-and-White porcelain. *Archaeometry* **2021**, *63*, 194–203. [CrossRef]
27. Li, X.; Dong, W.; Bao, Q.; Yang, Y.; Zhao, T.; Liu, L.; Zhou, J. Maximization of the blue-white contrast of ancient porcelain decorations from Jingdezhen imperial kiln by Co-spinel formation. *J. Eur. Ceram. Soc.* **2024**, *44*, 6697–6707. [CrossRef]
28. Van Pevenage, J.; Lauwers, D.; Herremans, D.; Verhaeven, E.; Vekemans, B.; De Clercq, W.; Vincze, L.; Moens, L.; Vandenabeele, P. A Combined Spectroscopic Study on Chinese Porcelain Containing Ruan-Cai Colours. *Anal. Methods* **2014**, *6*, 387–394. [CrossRef]
29. Colomban, P.; Zhang, Y.; Zhao, B. Non-invasive Raman analyses of huafalang and related porcelain wares. Searching for evidence for innovative pigment technologies. *Ceram. Int.* **2017**, *43*, 12079–12088. [CrossRef]
30. Giannini, R.; Freestone, I.; Shortland, A.J. European cobalt sources identified in the production of Chinese *Famille rose* porcelain. *J. Archaeol. Sci.* **2017**, *80*, 27–36. [CrossRef]
31. Colomban, P.; Gironda, M.; Vangu, D.; Kırmızı, B.; Zhao, B.; Cochet, V. The technology transfer from Europe to China in the 17th–18th centuries: Non-invasive on-site XRF and Raman analyses of Chinese Qing Dynasty enameled masterpieces made using European ingredients/recipes. *Materials* **2021**, *14*, 7434. [CrossRef]
32. Colomban, P.; Gironda, M.; Simsek Franci, G.; d'Abrigeon, P. Distinguishing Genuine Imperial Qing Dynasty Porcelain from Ancient Replicas by On-site Noninvasive XRF and Raman Spectroscopy. *Materials* **2022**, *15*, 5747. [CrossRef]
33. Colomban, P.; Simsek Franci, G.; Gironda, M.; d'Abrigeon, P.; Schuhmacher, A.-C. pXRF Data Evaluation Methodology for On-Site Analysis of Precious Artifacts: Cobalt Used in the Blue Decoration of Qing Dynasty Overglazed Porcelain Enameled at Customs District (Guangzhou), Jingdezhen and Zaobanchu (Beijing) Workshops. *Heritage* **2022**, *5*, 1752–1778. [CrossRef]
34. Colomban, P.; Ngo, A.-T.; Fournery, N. Non-invasive Raman Analysis of 18th Century Chinese Export/Armorial Overglazed Porcelain: Identification of the Different Enameling Technology. *Heritage* **2022**, *5*, 233–259. [CrossRef]
35. Colomban, P.; Simsek Franci, G.; Burlot, J.; Gallet, X.; Zhao, B.; Clais, J.B. Non-Invasive on-Site pXRF Analysis of Coloring Agents, Marks and Enamels of Qing Imperial and Non-Imperial Porcelain. *Ceramics* **2023**, *6*, 447–474. [CrossRef]
36. Colomban, P.; Liem, N.Q.; Sagon, G.; Tinh, H.X.; Hoành, T.B. Microstructure, composition and processing of 15th century Vietnamese porcelains and celadons. *J. Cult. Herit.* **2003**, *4*, 187–197. [CrossRef]
37. Colomban, P.; Sagon, G.; Huy, L.Q.; Liem, N.Q.; Mazerolles, L. Vietnamese (15th Century) blue-and-white tam thai and luster porcelains/stonewares: Glaze composition and decoration techniques. *Archaeometry* **2004**, *46*, 125–136. [CrossRef]
38. Simsek, G.; Colomban, P.; Wong, S.; Zhao, B.; Rougeulle, A.; Liem, N.Q. Toward a fast non-destructive identification of pottery: The sourcing of 14th–16th century Vietnamese and Chinese ceramic shards. *J. Cult. Herit.* **2015**, *16*, 159–172. [CrossRef]
39. Xu, W.; Cui, J.; Qin, D.; Jiang, J.; Zou, F. The Formulae and Techniques Analysis of the Yuan-Dynasty White Porcelains Unearthed in the Kiln Site of Hongguang Ceramics Works of Luomaqiao, Jingdezhen. *Palace Mus. J.* **2017**, *189*, 124–143. [CrossRef]

40. Yu, T.; Liu, M.; Ren, L.; Gao, Q.; Zha, Y.; Xu, Z. EDXRF Analysis on the Composition of Yuxi Kiln Blue and White Porcelain in Yunnan Province. *Taoci Yanjiu (Ceram. Stud.)* **2020**, *35*, 89–92. (In Chinese) [CrossRef]
41. Chen, Y.; Guo, Y.; Zhao, G. A Study of Yuan Blue-and-White Porcelain from the Yuxi and Jianshui Kilns. *Zhongguo Taoci* **1989**, *6*, 56–62. (In Chinese)
42. Chen, Y.; Guo, Y.; Chen, H. Sources of Cobalt Pigment Used on Yuan Blue and White Porcelain Wares. *Orient. Art* **1994**, *40*, 24–35.
43. Chen, L.; Dong, X. Jianshui ciyao diaocha yu tantao [Investigation and discussion of the Jianshui kilns]. In *Zhongguo Gu Taoci Yanjiu*; Zhongguo Gu Taoci Xuehui, Ed.; Zijincheng Chubanshe: Beijing, China, 2007; Volume 13, pp. 93–94. (In Chinese)
44. Shih, C.-F. Yunnan diqu qinghua ciqi de bianqian: Jian tan qi yu Jiangxi Jingdezhen he Yuenan qinghua ci de guanlian (The Development of Yunnan Blue-and-White and Its Relationships with Jiangxi Jingdezhen and Vietnamese Blue-and-White Wares). *Taida J. Art Hist.* **2008**, *25*, 171–270. (In Chinese)
45. Zhang, B. (Ed.) *Zhongguo Chutu Ciqi Quanji (Complete Collection of Ceramic Art Unearthed in China)*; Science Press: Beijing, China, 2008; Volume 16. (In Chinese)
46. Wu, B. *Nanzhong Diandai: Xijian Yunnan Qinghua Cipian Biaoben Jilu (Nanzhong Diandai: A Record of Rare Yunnan Blue-and-White Porcelain Sherd Specimens)*; Yunnan University Press: Kunming, China, 2024. (In Chinese)
47. Shanghai People's Fine Arts Publishing House (Ed.) *Chūgoku Tōji Zenshū*; Volume 29: Yunnan Tōji; Minobi: Kyoto, Japan, 1985.
48. Yunnan Sheng Wenwu Kaogu Yanjiusuo; Honghe Zhou Wenwu Guanlisuo; Gejiu Shi Bowuguan. Gejiu Wanglinzhai Xiaomanpo mudi fajue baogao (Excavation Report of the Xiaomanpo Cemetery at Wanglinzhai, Gejiu). In *Yunnan Kaogu Baogao Ji (II) (Yunnan Archaeological Reports II)*; Yang, D., Yunnan Sheng Wenwu Kaogu Yanjiusuo, Eds.; Yunnan Keji Chubanshe: Kunming, China, 2006; pp. 159–192. (In Chinese)
49. Butterfields Auctioneers Corporation (Ed.) *Treasures from the Hoi An Hoard: Important Vietnamese Ceramics from a Late 15th/Early 16th Century Cargo*; Butterfields Auctioneers Corporation: San Francisco, CA, USA, 2000; Volume 2.
50. Stevenson, J.; Guy, J. *Vietnamese Ceramics: A Separate Tradition*; Art Media Resources: Chicago, IL, USA, 1997.
51. Bùi, M.T.; Nguyễn-Long, K. *Gốm Hoa Lam Việt Nam (Vietnamese Blue and White Ceramics)*; Nguyen, K.L., Translator; Social Sciences Publishing House: Hanoi, Vietnam, 2001. (In Vietnamese)
52. Tăng, B.H. (Ed.) *Gốm Chu Đậu (Chu Dau Ceramics of Vietnam)*; Museum of Hai Hung Province: Hai Hung, Vietnam, 1993. (In Vietnamese)
53. Nguyen-Long, K. Ba Dinh Excavation: Thang Long Imperial Citadel. *Arts Asia* **2007**, *37*, 114–122.
54. Bùi, M.T. An Overview of Vietnamese Polychrome Ceramics in the Context of Asian History and Culture (Translated by Zhang, X.). *Palace Mus. J.* **2020**, *221*, 65–88. (In Chinese)
55. Zhao, W.; Tung, B.X. Archaeological Work in the Central Area of Imperial Citadel of Thang Long-Hanoi, Vietnam. *Acad. J. Humanit. Social. Sci.* **2021**, *4*, 115–125. [CrossRef]
56. van Orsoy de Flines, E.W. *Guide to the Ceramic Collection of the Museum Pusat Jakarta*; First published 1949 in Dutch; Museum Pusat: Jakarta, Indonesia, 1972.
57. Li, L.; Feng, S.L.; Feng, X.Q.; Xu, Q.; Yan, L.T.; Ma, B.; Huo, H. Study on the chemical composition features of Longquan celadon excavated from the Chuzhou site of Huai'an City in Jiangsu Province by EDXRF. *Chin. Phys. C* **2011**, *35*, 689. [CrossRef]
58. Zhu, T.Q.; Wu, F.; Wan, J.L.; Wang, M.; Ahamed, B.K.; Liu, C.J.; Wang, Z. Study on the material and manufacturing technology of different types of Longquan ware imitations from Dapu Kiln of Guangdong Province in the Ming Dynasty of China (ad 1368–1644). *Archaeometry* **2018**, *60*, 42–53. [CrossRef]
59. Edwards, H.G.; Vandenabeele, P.; Colomban, P. *Raman Spectroscopy in Cultural Heritage Preservation*; Springer: Berlin/Heidelberg, Germany, 2023. [CrossRef]
60. Colomban, P. Full Spectral Range Raman Signatures Related to Changes in Enamelling Technologies from 18th to the 20th Century: Guidelines, Effectiveness and Limitations of the Raman Analysis. *Materials* **2022**, *15*, 3158. [CrossRef]
61. Kamura, S.; Tani, T.; Matsuo, H.; Onaka, Y.; Fujisawa, T.; Unno, M. New probe for porcelain glazes by luminescence at Near-Infrared excitation. *ACS Omega* **2021**, *6*, 7829–7833. [CrossRef]
62. Onaka, Y.; Matsuo, H.; Aoyama, A.; Ohto, K.; Yamada, Y.; Fujisawa, T.; Unno, M. Near-Infrared Luminescence from Porcelain Glazes Originates from Neodymium Ion. *J. Phys. Chem. C* **2026**, *130*, 1357–1362. [CrossRef]
63. Janssens, K. *Modern Methods for Analysing Archaeological and Historical Glass*; John Wiley and Sons Ltd.: Chichester, UK, 2013; Volume 2.
64. Colomban, P. The on-site/remote Raman analysis with mobile instruments: A review of drawbacks and success in cultural heritage studies and other associated fields. *J. Raman Spectrosc.* **2012**, *43*, 1529–1535. [CrossRef]
65. Bezur, A.; Casadio, F. The analysis of porcelain using handheld and portable X-ray fluorescence spectrometers. In *Handheld XRF for Art and Archaeology*; Shugar, A.N., Mass, J.L., Eds.; Leuven University Press: Leuven, Belgium, 2012; pp. 249–312. Available online: https://www.torrossa.com/en/resources/an/4815865#page=249 (accessed on 8 February 2026).

66. Ma, H.; Henderson, J.; Evans, J. The exploration of Sr isotopic analysis applied to Chinese glazes: Part one. *J. Archaeol. Sci.* **2014**, *50*, 551–558. [CrossRef]
67. Kimura, J. Maritime archaeological perspectives on seaborne trade in the South China Sea and East China Sea between the seventh and thirteenth Centuries. *Crossroads Stud. Hist. Exch. Relat. East. Asian World* **2016**, *11*, 47–61. Available online: https://ostasien-verlag.de/zeitschriften/crossroads/cr/pdf/CR_11_2015_047-061_Kimura.pdf (accessed on 8 February 2026).
68. Ha, S.T. The collection of Cu Lao Cham shipwreck at the Museum of History-Culture. *J. Sci. Technol. Dev.* **2014**, *17*, 75–82. (In Vietnamese) [CrossRef]
69. Zhang, B. (Ed.) *Zhongguo Chutu Ciqi Quanji (Complete Collection of Ceramic Art Unearthed in China)*; Science Press: Beijing, China, 2008; Volume 4. (In Chinese)
70. Ye, H.; Xia, Y.; Hu, C. Shexian chutu liang pi jiaocang Yuan ci jingpin (Fine Yuan Porcelains from Two Hoards Unearthed in Shexian). *Wenwu* **1988**, *5*, 85–88. (In Chinese)
71. Liu, X.; Bai, K. Jingdezhen Hutian yao kaocha jiyao (Summary of the Investigation of the Hutian Kiln in Jingdezhen). *Wenwu* **1980**, *11*, 39–49. (In Chinese)
72. Shih, C.-F. Mongyuan gongting zhong ciqi shiyong chutan (A Preliminary Study of the Use of Ceramics in the Mongol Yuan Court). *Taida J. Art. Hist.* **2003**, *15*, 173–179. (In Chinese)
73. Yuba, T. Fusitate yizhi chutu de Zhongguo taoci—1998–2001 nian yanjiu chengguo jieshao (The Chinese Ceramics Unearthed in the Fustat Ruins: An Overview of the 1998–2001 Research Results). *Palace Mus. J.* **2016**, *183*, 120–132. (In Chinese)
74. Jiang, J.; Gao, X.; Qin, D.; Weng, Y.; Jiang, X.; Wei, Y.; Li, X. The Excavation of the Kiln Site of the Ming and Qing Dynasties within Hongguang Porcelain Factory at Luomaqiao, Jingdezhen, Jiangxi. *Wenwu* **2020**, *11*, 4–78. (In Chinese) [CrossRef]
75. Hubei Provincial Bureau of Cultural Heritage (Ed.) *Zigui Miaoping*; pls. 82–83; Science Press: Beijing, China, 2003; p. 141. (In Chinese)
76. Mukai, K. Chronology of Si Satchanalai Glazed Ware, North-Central Thailand, Based on Material Found from Wrecksites. *Trade Ceram. Stud.* **2001**, *21*, 75–89. (In Japanese)
77. Gotuaco, L.; Tan, R.C.; Diem, A.I. *Chinese and Vietnamese Blue and White Wares Found in the Philippines*; Bookmark: Makati City, Philippines, 1997.
78. Demirsar Arli, B.; Simsek Franci, G.; Kaya, S.; Arli, H.; Colomban, P. Portable X-ray fluorescence (p-XRF) uncertainty estimation for glazed ceramic analysis: Case of Iznik tiles. *Heritage* **2020**, *3*, 1302–1329. [CrossRef]
79. Okinawa Kenritsu Maizō Bunkazai Sentā (Ed.) *Shurijō Kyō-no-uchi Ten: Bōeki Tōji kara Mita Daikōeki Jidai (Exhibition on Shuri Castle, Kyō-no-uchi: The Great Age of Trade as Seen Through Trade Ceramics)*; Okinawa Kenritsu Maizō Bunkazai Sentā: Nishihara, Japan, 2001. (In Japanese)
80. Burlot, J.; Gallet, X.; Simsek Franci, G.; Bellot-Gurlet, L.; Colomban, P. Non-invasive on-site pXRF analysis of coloring agents of under-and over-glazes: Variability and representativity of measurements on porcelain. *Colorants* **2023**, *2*, 42–57. [CrossRef]
81. Colomban, P.; Franci, G.S.; Gerken, M.; Gironda, M.; Mesqui, V. Chemical and Vibrational Criteria for Identifying Early Sèvres Factory Porcelain Productions. *Ceramics* **2024**, *7*, 1905–1927. [CrossRef]
82. Bruker. XRF Check—Information Depth. Available online: https://xrfcheck.bruker.com/InfoDepth (accessed on 9 August 2026).
83. Lawrence Berkeley National Laboratory. XRF Tables. Available online: https://xdb.lbl.gov/Section1/Table_1-2.pdf (accessed on 16 March 2026).
84. Kissin, S.A. Five-element (Ni-Co-As-Ag-Bi) veins. *Geosci. Can.* **1992**, *19*, 113–124. Available online: https://www.erudit.org/en/journals/geocan/1992-v19-n3-geocan_19_3/geocan19_3art02.pdf (accessed on 8 February 2026).
85. Berrie, B.H. Mining for color: New blues, yellows, and translucent paint. *Early Sci. Med.* **2015**, *20*, 308–334. [CrossRef]
86. Moskalyk, R.R.; Alfantazi, A.M. Review of present cobalt recovery practice. *Min. Metall. Explor.* **2000**, *17*, 205–216. [CrossRef]
87. Roberts, S.; Gunn, G. Cobalt. Cobalt. In *Critical Metals Handbook*; Gunn, G., Ed.; John Wiley & Sons: Hoboken, NJ, USA, 2014; pp. 122–149. [CrossRef]
88. Mudd, G.M.; Weng, Z.; Jowitt, S.M.; Turnbull, I.D.; Graedel, T.E. Quantifying the recoverable resources of by-product metals: The case of cobalt. *Ore Geol. Rev.* **2013**, *55*, 87–98. [CrossRef]
89. Hitzman, M.W.; Bookstrom, A.A.; Slack, J.F.; Zientek, M.L. *Cobalt—Styles of Deposits and the Search for Primary Deposits*; No. 2017-1155; US Geological Survey: Reston, VA, USA, 2017. [CrossRef]
90. Simsek, G.; Casadio, F.; Colomban, P.; Bellot-Gurlet, L.; Faber, K.T.; Zelleke, G.; Milande, V.; Moinet, E. On-site identification of early Böttger red stoneware made at Meissen using portable XRF: 1, body analysis. *J. Am. Cer. Soc.* **2014**, *97*, 2745–2754. [CrossRef]
91. Ruvalcaba Cornejo, C. Luminescence in Rare Earth Ion-doped oxide compounds. In *Luminescence—An Outlook on the Phenomena and Their Applications*; Thirumalai, J., Ed.; IntechOpen Book Series; IntechOpen: London, UK, 2016; Available online: https://www.intechopen.com/chapters/52672 (accessed on 20 January 2026).
92. Dieke, G.H. *Spectra and Energy Levels of Rare Earth Ions in Crystals*; Wiley Interscience: New York, NY, USA, 1968.

93. Edwards, H.G. Types of Porcelain and Their Elemental Oxide Compositions. In *Porcelain Analysis and Its Role in the Forensic Attribution of Ceramic Specimens*; Springer International Publishing: Cham, Switzerland, 2021; pp. 165–196. [CrossRef]
94. Bersani, D.; Lottici, P.P. Raman spectroscopy of minerals and mineral pigments in archaeometry. *J. Raman Spectrosc.* **2016**, *47*, 499–530. [CrossRef]
95. Colomban, P.; Treppoz, F. Identification and differentiation of ancient and modern European porcelains by Raman macro-and micro-spectroscopy. *J. Raman Spectrosc.* **2001**, *32*, 93–102. [CrossRef]
96. Colomban, P.; Milande, V. On-site Raman analysis of the earliest known Meissen porcelain and stoneware. *J. Raman Spectrosc.* **2006**, *37*, 606–613. [CrossRef]
97. Reinosa, J.J.; Del Campo, A.; Fernández, J.F. Indirect measurement of stress distribution in quartz particles embedded in a glass matrix by using confocal Raman microscopy. *Ceram. Int.* **2015**, *41*, 13598–13606. [CrossRef]
98. Colomban, P. Structure of oxide gels and glasses by infrared and Raman scattering: Part 2 Mullites. *J. Mater. Sci.* **1989**, *24*, 3011–3020. [CrossRef]
99. Michel, D.; Colomban, P.; Abolhassani, S.; Voyron, F.; Kahn-Harai, A. Germanium mullite: Structure and vibrational spectra of gels, glasses and ceramics. *J. Eur. Ceram. Soc.* **1996**, *16*, 161–168. [CrossRef]
100. Bost, N.; Duraipandian, S.; Guimbretière, G.; Poirier, J. Raman spectra of synthetic and natural mullite. *Vibr. Spectrosc.* **2016**, *82*, 50–52. [CrossRef]
101. Colomban, P.; Sagon, G.; Faurel, X. Differentiation of antique ceramics from the Raman spectra of their coloured glazes and paintings. *J. Raman Spectrosc.* **2001**, *32*, 351–360. [CrossRef]
102. Sacco, A.; Mandrile, L.; Tay, L.L.; Itoh, N.; Raj, A.; Moure, A.; Del Campo, A.; Fernandez, J.F.; Paton, K.R.; Wood, S.; et al. Quantification of titanium dioxide (TiO_2) anatase and rutile polymorphs in binary mixtures by Raman spectroscopy: An inter-laboratory comparison. *Metrologia* **2023**, *60*, 055011. [CrossRef]
103. Sun, J.; Wu, Z.; Cheng, H.; Zhang, Z.; Frost, R.L. A Raman spectroscopic comparison of calcite and dolomite. *Spectrochim. Acta Part A Mol. Biomol. Spectrosc.* **2014**, *117*, 158–162. [CrossRef]
104. Swamy, V.; Dubrovinsky, L.S.; Tutti, F. High-temperature Raman spectra and thermal expansion of wollastonite. *J. Am. Ceram. Soc.* **1997**, *80*, 2237–2247. [CrossRef]
105. Richet, P.; Mysen, B.O.; Ingrin, J. High-temperature X-ray diffraction and Raman spectroscopy of diopside and pseudowollastonite. *Phys. Chem. Miner.* **1998**, *25*, 401–414. [CrossRef]
106. De Aza, P.N.; Santos, C.; Pazo, A.; De Aza, S.; Cusco, R.; Artús, L. Vibrational properties of calcium phosphate compounds. 1. Raman spectrum of β-tricalcium phosphate. *Chem. Mater.* **1997**, *9*, 912–915. [CrossRef]
107. Colomban, P.; Maggetti, M.; d'Albis, A. Non-invasive Raman identification of crystalline and glassy phases in a 1781 Sèvres Royal Factory soft paste porcelain plate. *J. Eur. Ceram. Soc.* **2018**, *38*, 5228–5233. [CrossRef]
108. Edwards, H.G.; Colomban, P.; Bowden, B. Raman spectroscopic analysis of an English soft-paste porcelain plaque-mounted table. *J. Raman Spectrosc.* **2004**, *35*, 656–661. [CrossRef]
109. Heimann, R.B. Calcium Phosphate in Soft-Paste Porcelain: Bone China. In *Calcium Phosphate: Structure, Synthesis, Properties, and Applications*; Heimann, R.B., Ed.; Nova Biomedical: Waltham, MA, USA, 2012; pp. 467–475.
110. Wu, H.; Li, H.; Wang, Y.; He, P.; Li, Z.; Ma, Q. Was bone used in the glaze of the ancient Qiong kilns for the production of tang dynasty opaque glaze celadon? *J. Eur. Ceram. Soc.* **2025**, *45*, 117017. [CrossRef]
111. Hou, J.; Pradell, T.; Li, Y.; Miao, J. Jun ware glazes: Chemistry, nanostructure and optical properties. *J. Eur. Ceram. Soc.* **2018**, *38*, 4290–4302. [CrossRef]
112. Colomban, P. Polymerization degree and Raman identification of ancient glasses used for jewelry, ceramic enamels and mosaics. *J. Non-Crystall. Solids* **2003**, *323*, 180–187. [CrossRef]
113. Colomban, P.; Paulsen, O. Non-destructive determination of the structure and composition of glazes by Raman spectroscopy. *J. Am. Ceram. Soc.* **2005**, *88*, 390–395. [CrossRef]
114. Colomban, P.; Tournie, A.; Bellot-Gurlet, L. Raman identification of glassy silicates used in ceramics, glass and jewellery: A tentative differentiation guide. *J. Raman Spectrosc.* **2006**, *37*, 841–852. [CrossRef]
115. Kusano, Y.; Fujii, T.; Takada, J.; Fukuhara, M.; Doi, A.; Ikeda, Y.; Takano, M. Epitaxial Growth of ϵ-Fe2O3 on Mullite Found through Studies on a Traditional Japanese Stoneware. *Chem. Mater.* **2008**, *20*, 151–156. [CrossRef]
116. Kusano, Y.; Nakata, H.; Peng, Z.; Maki, R.S.; Ogawa, T.; Fukuhara, M. Studying and utilizing traditional technologies: Microstructure and formation mechanism of ε-Fe2O3 on traditional Japanese Bizen Stoneware. *ACS Appl. Mater. Interfaces* **2021**, *13*, 38491–38498. [CrossRef]
117. Dejoie, C.; Sciau, P.; Li, W.; Noé, L.; Mehta, A.; Chen, K.; Luo, H.; Kunz, M.; Tamura, N.; Liu, Z. Learning from the past: Rare ε-Fe2O3 in the ancient black-glazed Jian (Tenmoku) wares. *Sci. Rep.* **2014**, *4*, 4941. [CrossRef]
118. Wang, L.; Wang, Y.; Zhang, M.; Li, Q.; Wu, J.; Liu, Z.; Wei, X. Three-dimensional microstructure of ε-Fe_2O_3 crystals in ancient Chinese sauce glaze porcelain revealed by focused ion beam scanning electron microscopy. *Anal. Chem.* **2019**, *91*, 13054–13061. [CrossRef]

119. Tao, S.; Liu, S.; Yuan, Y.; Dong, J.; Li, Q. A Microstructural and Compositional Study of ε-Fe2O3 Crystals in the Hare's Fur Jian Ware. *Crystals* **2022**, *12*, 367. [CrossRef]
120. Wang, M.; Wang, T.; Wang, F.; Hole, C.; Cao, J.; Zhu, J.; Zhang, P.; Shi, P.; Sciau, P. Raman study of rusty oil spotted glaze produced in Linfen kilns (Shanxi province, AD 1115–1368). *J. Raman Spectrosc.* **2022**, *53*, 582–592. [CrossRef]
121. Guan, M.; Guo, Y.; Kang, B.; Wang, M.; Li, G.; Zheng, Y.; Ding, Y.; Wang, M.; Wood, N.; Lei, Y.; et al. Uncovering the mystery of Al (III) doping of ε-Fe2O3 in the ancient high-iron black-brown glaze. *J. Am. Ceram. Soc.* **2024**, *107*, 522–533. [CrossRef]
122. Wang, T.; Xia, S.; Ren, Z.; Hole, C.; Wang, F.; Zhu, J.; Sciau, P. Study on the morphology and structure of ε-Fe_2O_3 crystals in Chinese sauce wares (960–1279 CE). *npj Herit. Sci.* **2025**, *13*, 431. [CrossRef]
123. Huber, G. Solid-state laser materials. In *Laser sources and Applications*; CRC Press: Boca Raton, FL, USA, 1997; pp. 141–162.
124. Pezzotti, G. In situ study of fracture mechanisms in advanced ceramics using fluorescence and Raman microprobe spectroscopy. *J. Raman Spectrosc.* **1999**, *30*, 867–875. [CrossRef]
125. Sinclair, R.; Young, R.J.; Martin, R.D.S. Determination of the axial and radial fibre stress distributions for the Broutman test. *Compos. Sci. Technol.* **2004**, *64*, 181–189. [CrossRef]
126. Gouadec, G.; Colomban, P.; Piquet, N.; Trichet, M.F.; Mazerolles, L. Raman/Cr^{3+} fluorescence mapping of a melt-grown Al_2O_3/$GdAlO_3$ eutectic. *J. Eur. Ceram. Soc.* **2005**, *25*, 1447–1453. [CrossRef]
127. Redonnet, J.; Simsek-Franci, G.; Colomban, P. Non-Invasive Rayleigh, Raman, and Chromium-Fluorescence Study of Phase Transitions: β-Alumina into γ-Alumina 'Single' Crystal and Then to α-Alumina. *Materials* **2025**, *18*, 4682. [CrossRef]
128. Iqbal, Y.; Lee, W.E. Microstructural evolution in triaxial porcelain. *J. Am. Ceram. Soc.* **2000**, *83*, 3121–3127. [CrossRef]
129. Low, I.M.; McPherson, R. The origins of mullite formation. *J. Mater. Sci.* **1989**, *24*, 926–936. [CrossRef]
130. Colomban, P.; Mazerolles, L. SiO_2-Al_2O_3 phase diagram and mullite non-stoichiometry of sol-gel prepared monoliths: Influence on mechanical properties. *J. Mater. Sci. Lett.* **1990**, *9*, 1077–1079. [CrossRef]
131. Schneider, H.; Schreuer, J.; Hildmann, B. Structure and properties of mullite—A review. *J. Eur. Ceram. Soc.* **2008**, *28*, 329–344. [CrossRef]
132. Lee, W.E.; Souza, G.P.; McConville, C.J.; Tarvornpanich, T.; Iqbal, Y. Mullite formation in clays and clay-derived vitreous ceramics. *J. Eur. Ceram. Soc.* **2008**, *28*, 465–471. [CrossRef]
133. Duval, D.J.; Risbud, S.H.; Shackelford, J.F. Mullite. In *Ceramic and Glass Materials: Structure, Properties and Processing*; Springer: Boston, MA, USA, 2008; pp. 27–39.
134. Schneider, H.; Fischer, R.X.; Schreuer, J. Mullite: Crystal structure and related properties. *J. Am. Ceram. Soc.* **2015**, *98*, 2948–2967. [CrossRef]

Disclaimer/Publisher's Note: The statements, opinions and data contained in all publications are solely those of the individual author(s) and contributor(s) and not of MDPI and/or the editor(s). MDPI and/or the editor(s) disclaim responsibility for any injury to people or property resulting from any ideas, methods, instructions or products referred to in the content.